

1 **A global view of the stratospheric background, volcanic and**  
2 **wildfire aerosol in the CALIOP era (2006 – 2023)**

3 Bengt G. Martinsson, Johan Friberg, and Moa K. Sporre

4 Department of Physics, Lund University, Lund, Sweden

5 *Correspondence to:* Bengt G. Martinsson (bengt.martinsson@fysik.lu.se)

6 **Abstract.** This study deals with the stratospheric aerosol during the 17 years of lidar  
7 measurements with CALIOP aboard the CALIPSO satellite. To obtain extinction from the  
8 backscattering measurements, we estimated the lidar ratios of the main aerosol  
9 injections into the stratosphere. The stratospheric background is estimated by making a  
10 subdivision of the stratosphere into nine parts, spanned by three latitude and altitude  
11 intervals, reaching background conditions individually at different times. The extracted  
12 background estimate shows excellent agreement with SAGE II solar occultation  
13 measurements in the volcanically quiescent period 1998 - 2000. Our results show that  
14 70% of the background aerosol in the deep Brewer-Dobson (dBD) branch is formed  
15 above 19 km altitude, indicating strong influence of carbonyl sulfide on the  
16 stratospheric background aerosol. The stratosphere was clearly affected by 15 volcanic  
17 eruptions and 5 wildfires. Their combined aerosol load affected the Southern  
18 extratropics, tropics and Northern extratropics almost equally, and the altitude  
19 distribution shows that the shallow Brewer-Dobson branch was most affected (43%)  
20 followed by the dBD (31%) and lowermost stratosphere (26%). The most important  
21 events in order of maximum AOD were the Hunga Ha’apai eruption (2022), Australian  
22 wildfires (2019-20) and the eruptions of Raikoke (2019), Sarychev (2009) and Nabro  
23 (2011). These events induced strong variability in the yearly average global stratospheric  
24 aerosol optical depth (AOD), which ranged from 0.0057 (background) to 0.016. CALIOP  
25 provided invaluable data for stratospheric aerosol climatologies during its 17 years of  
26 operation.

## 27 **1. Introduction**

28 Tropospheric air, containing aerosol particles and the sulfurous aerosol precursor gases  
29 carbonyl sulfide (OCS) and sulfur dioxide (SO<sub>2</sub>), enter the stratosphere across the  
30 tropical tropopause. These constituents form the stratospheric background aerosol  
31 (Kremser et al., 2016), an aerosol layer that is located above 20 km altitude in the  
32 tropics, and lower in the extratropics, containing water-soluble sulfur-rich particles  
33 (Junge et al., 1961). Additional aerosol, that can be classified as background due to its  
34 diffuse nature, originates from the Asian Tropopause Aerosol Layer (ATAL), an aerosol  
35 layer between 13 – 18 km altitude over Asia (Vernier et al., 2015). The stratospheric  
36 background aerosol contains sulfate, water, organics, and minor traces of tropospheric  
37 aerosol and extraterrestrial material (Martinsson et al., 2005; Murphy et al., 2007;  
38 Kremser et al., 2016; Martinsson et al., 2019).

39 The stratospheric aerosol load is highly variable due to special aerosol events  
40 connected to volcanism (Bauman et al., 2003; Vernier et al., 2009; Solomon et al., 2011;  
41 Andersson et al., 2015) and wildfires (Fromm et al., 2010; Baars et al., 2019; Ohneiser et  
42 al., 2020; Peterson et al., 2021; Martinsson et al., 2022; Solomon et al., 2022; Friberg et  
43 al, 2023, Peterson et al., 2025), which inject copious amounts of aerosol and precursor  
44 gases affecting the stratospheric aerosol for months up to several years (Friberg et al.,  
45 2018). These aerosol events induce a variability that needs to be accounted for in  
46 climate models. From 1979, the satellite measurement era, the most important  
47 volcanic eruptions, El Chichon in 1982 and Mt. Pinatubo (1991), caused a maximum  
48 global 3-month average effective radiative forcing of -2 and -3 W/m<sup>2</sup>, respectively  
49 (Schmidt et al., 2018). After a period of low volcanic influence on the stratosphere  
50 around the turn of the millennium, many volcanic eruptions and wildfires have affected  
51 the aerosol in the stratosphere. The most important are the 2019-20 Australian wildfires  
52 and the eruptions of Sarychev (2009), Raikoke (2019) and Hunga Ha'apai (2022).

53 Fresh wildfire aerosol particles contain black carbon and a dominating fraction of  
54 organics (Garofalo et al., 2019), where the latter is rapidly lost (half-life 10 days) in the  
55 stratosphere due to photolysis (Martinsson et al., 2022). The composition of volcanic  
56 stratospheric aerosol particles varies. SO<sub>2</sub>-rich volcanic emissions, like the 2008

57 eruption of Kasatochi, are dominated by sulfate, some organics and a minor fraction of  
58 ash (Martinsson et al., 2009, Andersson et al., 2013; Friberg et al., 2014). On the other  
59 hand, SO<sub>2</sub>-poor eruptions, like that of Puyehue-Cordón Caulle in 2011, are dominated  
60 by ash (Clarisse et al., 2013). Steam-boosted eruptions of submarine volcanoes (Mastin  
61 et al., 2024), like the 2022 eruption of Hunga Ha’apai, can result in a stratospheric  
62 aerosol with a strong contribution from sea salt (Martinsson et al., 2025).

63 From the beginning of extensive satellite data in the late 1970s the stratospheric aerosol  
64 load has usually been measured using solar occultation (Sato et al., 1993). GloSSAC  
65 (Global Space-based Stratospheric Aerosol Climatology), a later construction of a  
66 continuous record of optical properties of stratospheric aerosol spanning 1979 to  
67 present, has a core of solar occultation measurement with the notable 22 year era of  
68 SAGE II continuing a few years of solar occultation measurement by SAM II and SAGE I  
69 (Thomason et al., 2018). Solar occultation became unavailable during 2005 – 2017. To  
70 continue the GloSSAC record, other satellite-based measurements were deployed. The  
71 limb scatter instrument OSIRIS (Rieger et al., 2015) and the lidar CALIOP (Cloud-Aerosol  
72 Lidar with Orthogonal Polarization) (Winker et al., 2010) were, after substantial  
73 recalibration (Thomason et al., 2018, Kovilakam et al., 2020, Kovilakam et al., 2023),  
74 used to bridge the gap to obtain continuous time series of stratospheric aerosol  
75 properties. Mixing data from many sources that are relying on different measurement  
76 principles is however complex, as pointed out by Thomason et al. (2018). We will return  
77 to this matter in the discussion section.

78 This work deals with the stratospheric aerosol in the CALIOP era, spanning the 17-year  
79 period 2006-06-12 to 2023-06-30. CALIOP data (level 1B, version 4-51) is corrected for  
80 attenuation, and the lidar ratio is estimated for the stratospheric aerosol resulting from  
81 12 volcanic eruptions and wildfires. The stratosphere from the tropopause to 35 km  
82 altitude is divided into three altitude and three latitude parts, in total nine parts, where  
83 the backscattering of the background stratospheric aerosol is identified and its sources  
84 discussed. By subtraction of the signal from the background aerosol, the backscattering  
85 from major stratospheric aerosol events is obtained. This is converted to AOD using the  
86 estimated lidar ratios. We find that global average aerosol backscattering intensity  
87 exceeded the background by 55% in the 17 years studied. The strongest influence from

88 volcanism and wildfires was in 2022 and 2023 due to the submarine Hunga Ha’apai  
89 eruption. The second strongest occurred in 2020 due to the Australian wildfires,  
90 followed by 2009 (Sarychev eruption) and 2019 (mainly the Raikoke eruption). 2013 was  
91 a year when the entire stratosphere was close to background conditions. Finally, we  
92 discuss the validity of lidar data in comparison with the more established data based on  
93 solar occultation.

## 94 **2. Methods**

95 This paper is based on measurements with the CALIOP lidar instrument aboard the  
96 CALIPSO (Cloud-Aerosol Lidar and Infrared Pathfinder Satellite Observation) satellite  
97 that completed approximately 15 orbits between latitudes -82 and 82° each day.

### 98 ***2.1 CALIOP properties and methods applied***

99 CALIOP with a laser of 532 nm wavelength produced vertical profiles of backscattering  
100 intensity from air molecules, aerosol particles and cloud drops from the ground up to 35  
101 km altitude with high vertical resolution depending on altitude. In the altitude ranges <  
102 8.2, 8.2 - 20.2, 20.2 – 30.1 and >30.1 km the vertical resolution is 30, 60, 180 and 300 m,  
103 respectively (Winker et al., 2007, 2010). Here we use data only from the stratosphere,  
104 where the tropopause altitude according to MERRA-2 reanalysis (Modern-Era  
105 Retrospective analysis for Research and Applications) (Gelaro et al., 2017) was used to  
106 discriminate data from the troposphere. Only data recorded during nighttime were used  
107 in the general evaluation concerning all the CALIOP data available (Friberg et al., 2018;  
108 Martinsson et al., 2022), implying that data will be missing at high latitudes for part of  
109 the year with the strongest influence at the summer solstice. Data are also missing at  
110 high latitudes mainly in the southern hemisphere due to influence from polar  
111 stratospheric clouds. The data were extrapolated linearly to cover all the way to 80°  
112 latitude in both hemispheres. In the global perspective used here the fraction of the  
113 earth’s surface area affected by the extrapolation is 8.7% at the summer solstice and  
114 3.5% two months before/after that time. In most cases the quantitative impact on the  
115 global AOD is small, but in special cases, like the eruption of the Icelandic volcano

116 Grimsvötn (64° N) on 21 May 2011, the inability to measure at high latitudes causes  
117 larger quantitative errors (Andersson et al., 2015).

118 The evaluation is based on version 4-51 of CALIOP level 1B data (NASA/LARC/SD/ASDC,  
119 2024). Clouds within 3km above the tropopause were discriminated based on  
120 depolarization of the signal obtained from the CALIOP instrument, polar stratospheric  
121 clouds were discriminated based on temperature and data taken in the South Atlantic  
122 Anomaly are filtered out as explained in Friberg et al. (2018) and Martinsson et al.  
123 (2022). The backscatter data were corrected for attenuation by methodology described  
124 in Martinsson et al. (2022) and were first converted to extinction by the standard  
125 effective lidar ratio  $S = 50$  sr used for CALIOP (Kar et al., 2019). Volcanic eruptions and  
126 wildfires with lidar ratio deviating from 50 sr by more than 5% were corrected, see  
127 sections 2.3 and 3.4.

128 The stratospheric CALIOP level 3 product (Kar et al., 2019) and the data presented here  
129 are both based on the CALIOP level 1B data set but differ with respect to latitude-,  
130 longitude- and time-resolution, where CALIOP level 3 is based on monthly averages and  
131 we normally use a time-resolution of 1 – 8 days depending on issue investigated. These  
132 data sets also differ with respect to lidar ratios: CALIOP level 3 extinction is obtained  
133 based on a fixed lidar ratio of 50 sr, whereas we, when possible, estimate effective lidar  
134 ratios for aerosol from individual volcanic eruptions and wildfires as described in  
135 sections 2.3, 3.1 and 3.4. The notion “effective” relates to that CALIOP is affected by  
136 multiple scattering, implying that use of lidar ratios for measurements unaffected by  
137 multiple scattering, i.e., the true physical relation between extinction and  
138 backscattering of the aerosol studied, will result in overestimation the extinction (Prata  
139 et al., 2017; Martinsson et al., 2022). Another difference between CALIOP level 3 and  
140 our method is that we correct data for attenuation of the detected scattered light  
141 (Martinsson et al., 2022), which is important for identification and quantification of  
142 aerosol processes in wildfire aerosol (Martinsson et al., 2022; Friberg et al., 2023) and  
143 volcanic aerosol (Martinsson et al., 2025) and to obtain the AOD without influence from  
144 attenuation.

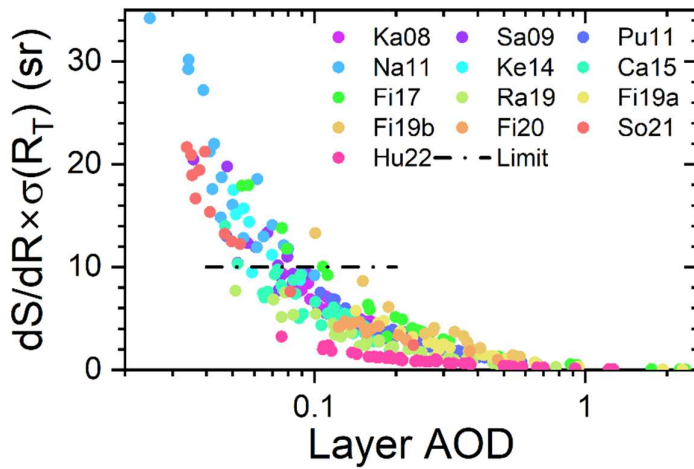
145 ***2.2 Estimation of the stratospheric background***

146 The stratospheric aerosol background can rarely be observed in the entire stratosphere.  
147 The last time the stratosphere was practically unaffected by injections from volcanic  
148 eruptions and wildfires for several years was a few years around the turn of the  
149 millennium (Solomon et al., 2011). Still, we need to find means to estimate the  
150 stratospheric background because we can estimate the lidar ratio of stratospheric  
151 injections from volcanic eruptions and wildfires (presented in next section) but not for  
152 the background aerosol. Injections from aerosol events seldom affect the entire  
153 stratosphere. Therefore, parts of the stratosphere can be in background conditions  
154 when other parts are affected by aerosol injections.

155 To study the background conditions, the stratosphere was subdivided into nine parts  
156 spanned by three altitude layers: the lowermost stratosphere (LMS, from the  
157 tropopause to the 380 K isentrope, where the latter was obtained from MERRA-2  
158 pressures and temperatures), the shallow Brewer-Dobson branch (sBD, between  
159 isentropes 380 and 470 K) and the deep Brewer-Dobson branch (dBD, from the 470 K  
160 isentrope to 35 km altitude), and three latitude regions: the Southern extratropics  
161 (latitudes -80 to -20°), the tropics (latitudes -20 to 20°) and the Northern extratropics  
162 (latitudes 20 to 80°)., Data were averaged over 8 days resulting in 46 observations per  
163 year in each of the nine stratospheric parts. To estimate the background conditions in  
164 this 17-year study, the averages of the three years with the lowest average  
165 backscattering of each 8-day period were formed. For two of the nine stratospheric  
166 parts, the tropical sBD and dBD, background conditions were rare, wherefore only the  
167 two lowest years were used in these two stratospheric parts. The method applied  
168 results in the minimum aerosol load observed during the 17-year period. This means  
169 that in addition to the tropospheric aerosol and precursor gases entering the  
170 stratosphere across the tropical tropopause in the large-scale stratospheric circulation,  
171 phenomena such as the ATAL (Vernier et al., 2015) and other exchanges across the  
172 extratropical tropopause are included in the background.

173 The extracted lowest 8-day values formed a seasonal pattern that was fitted by the sum  
174 of a constant and a sinusoidal function. These fits were used to express the average  
175 backscattering of the background aerosol in each of the nine stratospheric parts over  
176 the 17 years spanned by CALIOP measurements. The average backscattering converts

177 to AOD when multiplied with the lidar ratio. The fitted background was subtracted from  
 178 the measured total backscattering to form the backscattering from volcanic eruptions  
 179 and wildfires. These background-subtracted average backscattering data were  
 180 converted to AOD via the lidar ratios obtained from individual aerosol events, as  
 181 described in the next section.



182

183 **Figure 1.** Relation between the layer AOD and the measure on the uncertainty of the  
 184 lidar ratio estimation.  $dS/dR$  is the sensitivity of the lidar ratio ( $S$ ) to small shifts of the  
 185 target scattering ratio ( $R$ ) and  $\sigma(R_T)$  is the standard deviation of the target  $R$  of each  
 186 eruption or wildfire obtained horizontally beside each aerosol layer investigated. Layers  
 187 with uncertainty exceeding 10 sr (“limit”) are discarded in the following analysis.

188 **2.3 Lidar ratio**

189 The lidar ratio of the aerosol from the strongest volcanic eruptions and wildfires in the  
 190 period studied was estimated based on methodology described in Martinsson et al.  
 191 (2022), where individual dense aerosol layers are investigated. In that method a target  
 192 value in scattering ratio ( $R$ ) obtained horizontally beside the studied aerosol layer ( $R_T$ ) is  
 193 reached below the layer in an iterative procedure that results in an estimate of the  
 194 effective lidar ratio, while correcting for attenuation of the backscattered signal. The  
 195 effective lidar ratio obtained describes the average conditions of the entire layer where  
 196 the optical properties in principle can vary. However, the lidar ratio estimates are  
 197 obtained in dense aerosol layers, where the influence from background aerosol is small.

198 The uncertainty in the estimated lidar ratio depends on the AOD of the layer. A small  
199 change in the lidar ratio ( $S$ ) results in a substantial change in the scattering ratio ( $R$ )  
200 below a dense layer, i.e.,  $dS/dR$  is small for dense aerosol layers.  $dS/dR$  is obtained by  
201 shifting  $R$  slightly around  $R_T$ . There is also an uncertainty in how well  $R_T$  represents the  
202 aerosol beneath the layer. We estimate that uncertainty by the standard deviation of the  
203 scattering ratio ( $\sigma(R_T)$ ) obtained horizontally beside all the aerosol layers studied for  
204 each volcanic eruption or wildfire. This is thus based on the assumption that the aerosol  
205 horizontally beside and below the aerosol layer have the same standard deviation in  $R$ ,  
206 but the actual scattering ratios horizontally beside and below an individual layer are  
207 uncorrelated. The estimated uncertainty becomes  $dS/dR \times \sigma(R_T)$ . Figure 1 shows all  
208  $dS/dR \times \sigma(R_T)$  related to the AOD of all the estimations of the lidar ratio. The uncertainty in  
209 the lidar ratio estimate increases as the layer AOD decreases, hence a limit was set to  
210  $dS/dR \times \sigma(R_T) < 10$  sr to pass as a lidar ratio estimate. As a result, most estimates for  
211 three volcanic eruptions, 2011 Nabro (Na11), 2014 Kelut (Ke14), and 2021 Soufriere  
212 (So21), among the 12 eruptions and wildfires analyzed were lost, as illustrated in Figure  
213 1.

214 For simplicity all the CALIOP data were evaluated using the standard lidar ratio of  $S_0 =$   
215 50 sr in the general evaluation. In the study of individual aerosol layers (Figure 1) both  
216 the AOD based on the estimated lidar ratio and that based on  $S_0$  were computed, where  
217 the latter ( $AOD_{50}$ ) was used to obtain the deviation caused by using  $S_0$ . This deviation  
218 depends on the  $S/S_0$  ratio and  $AOD_{50}$ , where the effect of  $S/S_0$  is the dominant one  
219 except for very dense aerosol layers. The result from the general evaluation is corrected  
220 afterwards based on the ratio of  $S_0$  and the estimated  $S$ , see section 3.4.

### 221 **3. Results**

222 Here we will present the stratospheric aerosol from the troposphere to 35 km altitude  
223 and the latitude range  $-80$  to  $80^\circ$  in the era of lidar measurements by the CALIOP  
224 instrument aboard the CALIPSO satellite. CALIOP measured the backscattered intensity  
225 from a 532 nm laser beam, which can be converted to extinction by multiplying with the  
226 ratio of extinction to backscatter, i.e. the lidar ratio. Knowing the lidar ratio thus is  
227 central for quantification by obtaining AOD from CALIOP measurements. We developed

228 methodology to estimate the effective lidar ratio from CALIOP measurements, a  
 229 methodology that also corrects for attenuation of the laser signal (Martinsson et al.,  
 230 2022). Here we start by presenting the lidar ratio of the main aerosol events of the  
 231 CALIOP era before giving an overview of the AOD in the period studied. Then we  
 232 investigate separation of aerosol signals of aerosol events due to volcanic eruptions and  
 233 wildfires from signals due to stratospheric background aerosol. This is followed by  
 234 sections on corrections of AOD due to lidar ratio deviations from the commonly  
 235 assumed 50 sr, an overview of the AOD and a simplified estimate of the stratospheric  
 236 aerosol's radiative impact.

### 237 **3.1 Lidar ratio**

238 The main aerosol events affecting the stratosphere in the CALIOP era are presented in  
 239 Table 1. The methodology we use to estimate lidar ratios requires sufficiently dense  
 240 aerosol layers as described in section 2, implying that some of the events mentioned in  
 241 Table 1 are not suitable for the methodology. The lidar ratio was investigated for

242 **Table 1.** Major volcanic eruptions and wildfires affecting the stratospheric aerosol in the  
 243 CALIOP era.

	Date	Volcano/wildfire	Lat <sup>a</sup>	Lon <sup>b</sup>	SO <sub>2</sub> (Tg)	References
	<i>Volcanic eruptions</i>					
1	2006-05-20	Soufriere Hills (Su)	17°	-62.2°	0.2	Carn and Prata (2010)
2	2006-10-07	Rabaul (Rb)	-4°	152°	0.23	Carn et al. (2009)
3	2008-08-07	Kasatochi (Ka)	52°	-176°	1.7	Thomas et al. (2011)
4	2009-06-12	Sarychev (Sa)	48°	153°	1.2	Haywood et al. (2010)
5	2010-10-05	Merapi (Me)	-7°	110°	0.44	Surono et al. (2012)
6	2011-06-05	Puyehue-Cordón Caulle (Pu)	-40°	-72°	0.25	Clarisse et al. (2012)
7	2011-06-12	Nabro (Na)	13°	42°	1.5	Clarisse et al. (2012)
8	2014-02-13	Kelut (Ke)	-8°	112°	0.18	Li et al. (2017)
9	2015-04-23	Calbuco (Ca)	-41°	-73°	0.3	Pardini et al. (2018)
10	2018-07-27	Ambae (Am)	-15°	168°	0.36	Malinina et al. (2021)
11	2019-06-22	Raikoke (Ra)	48°	153°	1.5	Kloss et al. (2021)
12	2019-06-26	Ulawun (Ul)	-5°	151°	0.14	Kloss et al. (2021)
13	2019-08-03	Ulawun (Ul)	-5°	151°	0.3	Kloss et al. (2021)
14	2021-04-10	Soufriere (So)	13°	-61°	0.31	Taylor et al. (2023)
15	2022-01-15	Hunga Ha'apai (Hu)	-21°	175°	0.45	Carn et al. (2022)
	<i>Wildfires</i>					
16	2006-12-19	Australia (A1)	-37°	147°	-	McCarthy et al. (2012)

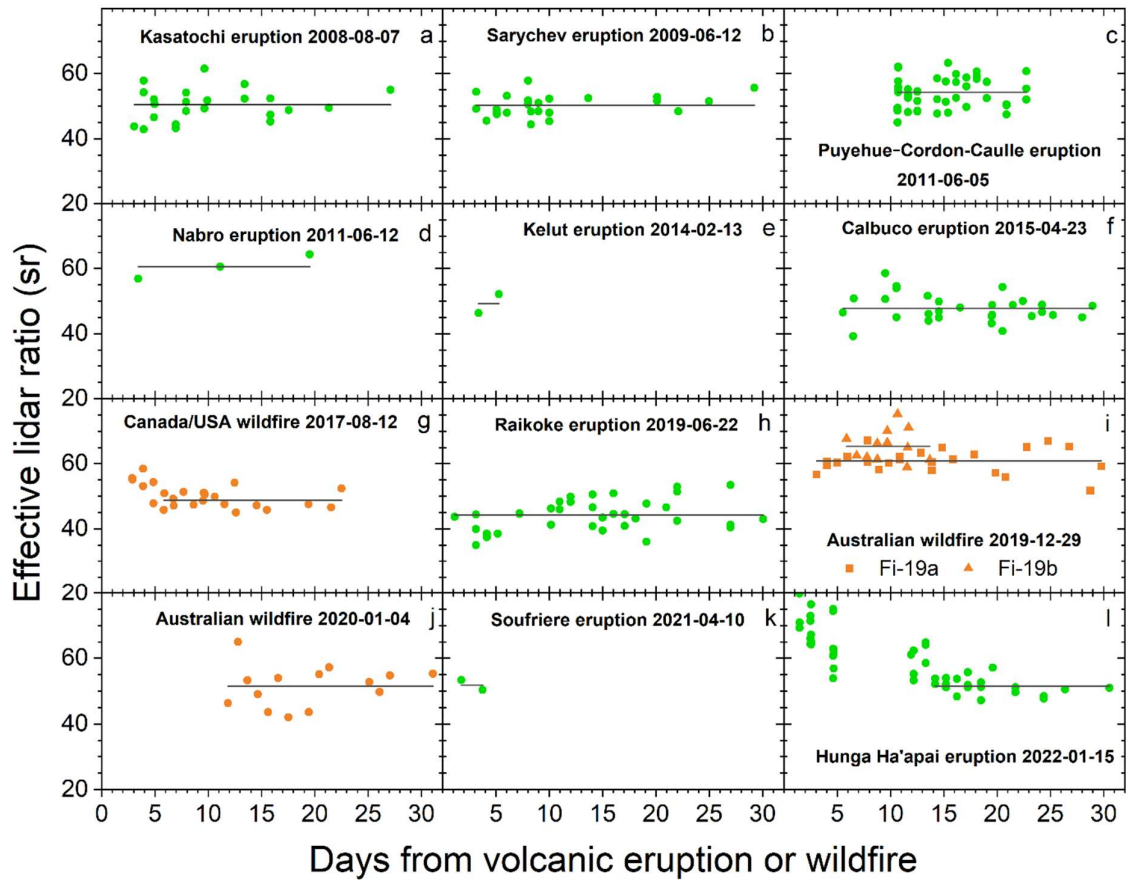
17	2009-02-07	Australia (A2)	-38°	146°	-	Cruz et al. (2012)
18	2017-08-12	Canada/USA (CU)	53°	-123°	-	Fromm et al. (2021)
19	2019-12-29	Australia (A3)	-37°	149°	-	Peterson et al. (2021)
20	2020-01-04	Australia (A4)	-37°	149°	-	Peterson et al. (2021)

244

245 stratospheric aerosol from nine volcanic eruptions and three wildfire events (Figure 2).  
 246 For some of these aerosol events the screening related to the uncertainty in the  
 247 estimated lidar ratio (Figure 1) resulted in few observations, namely for the 2011 Nabro,  
 248 2014 Kelut and the 2021 Soufriere eruptions. Most of the eruptions and wildfires display  
 249 a stable lidar ratio during the first month, whereas two of the events show an initial  
 250 decrease of the lidar ratio, the 2017 North American wildfire (Figure 2g) and the 2022  
 251 Hunga Ha'apai eruption (Figure 2l), towards a stable value.

252 Effective lidar ratios are presented here which are best suited for application to  
 253 measurements that, like CALIOP, are affected by multiple scattering (Martinsson et al.,  
 254 2022). Compared with previous estimates, the results presented here are approximately  
 255 20% lower than those of Prata et al. (2017) for the Kasatochi, Sarychev and Puyehue-  
 256 Cordon Caulle eruptions, who estimated lidar ratio for measurements that are not  
 257 affected by multiple scattering. Ohneiser et al. (2020) present Raman lidar measurements of  
 258 the 2019 Australian wildfire (Table 1) that are not affected by multiple scattering. On 2020-01-09  
 259 around 04:00 UTC (longitude -70.9, latitude -53.2)  $S = 76$  sr was obtained. The closest CALIOP  
 260 measurement in space and time that we evaluated was taken on the same day at 04:05,  
 261 position (-43.4, -53.1) with  $S = 75$  sr. The day before, at position (-57.2, -50.0)  $S = 70$  sr and the  
 262 day after at position (-55.0, -57.1)  $S = 71$  sr. All these three measurements belong to the fires  
 263 taking place last days of 2019, category B (outside the vortex) and are the three highest effective  
 264 lidar ratios obtained in this category.

265 Stratospheric aerosol resulting from most volcanic eruptions and wildfires have a lidar  
 266 ratio close to 50 sr, which is the commonly used lidar ratio for CALIOP data (Kar et al.,  
 267 2019). Notable exceptions with lidar ratio deviating by more than 5% from 50 sr are the  
 268 ash-dominated 2011 eruption of Puyehue-Cordón Caulle (Figure 2c), the 2019



269

270 **Figure 2.** Effective particle lidar ratios the first 30 days after a volcanic eruption or  
 271 wildfire with a line displaying the average of each event. All measurements concurring  
 272 with the condition  $dS/dR \times \sigma(R) < 10$  are displayed for a) Kasatochi eruption 2008-08-07,  
 273 b) Sarychev eruption 2009-06-12, c) Puyehue-Cordón-Caulle eruption 2011-06-05, d)  
 274 Nabro eruption 2011-06-12, e) Kelut eruption 2014-02-13, f) Calbuco eruption 2015-04-  
 275 23, g) Canada/USA wildfire 2017-08-12, h) Raikoke eruption 2019-06-22, i) Australian  
 276 wildfire, 2019-12-29 subdivided in part Fi-19a (observations in the vortex (Kablik et al.,  
 277 2020)) and Fi-19b (observations outside the vortex), j) Australian wildfire 2020-01-04, k)  
 278 Soufriere eruption 2021-04-10 and l) Hunga Ha'apai eruption 2022-01-15. The averages  
 279 include all data points except for the Canada/USA wildfire and the Hunga Ha'apai  
 280 eruption where the initial decline in the lidar ratio is not part of the average represented  
 281 by horizontal lines.

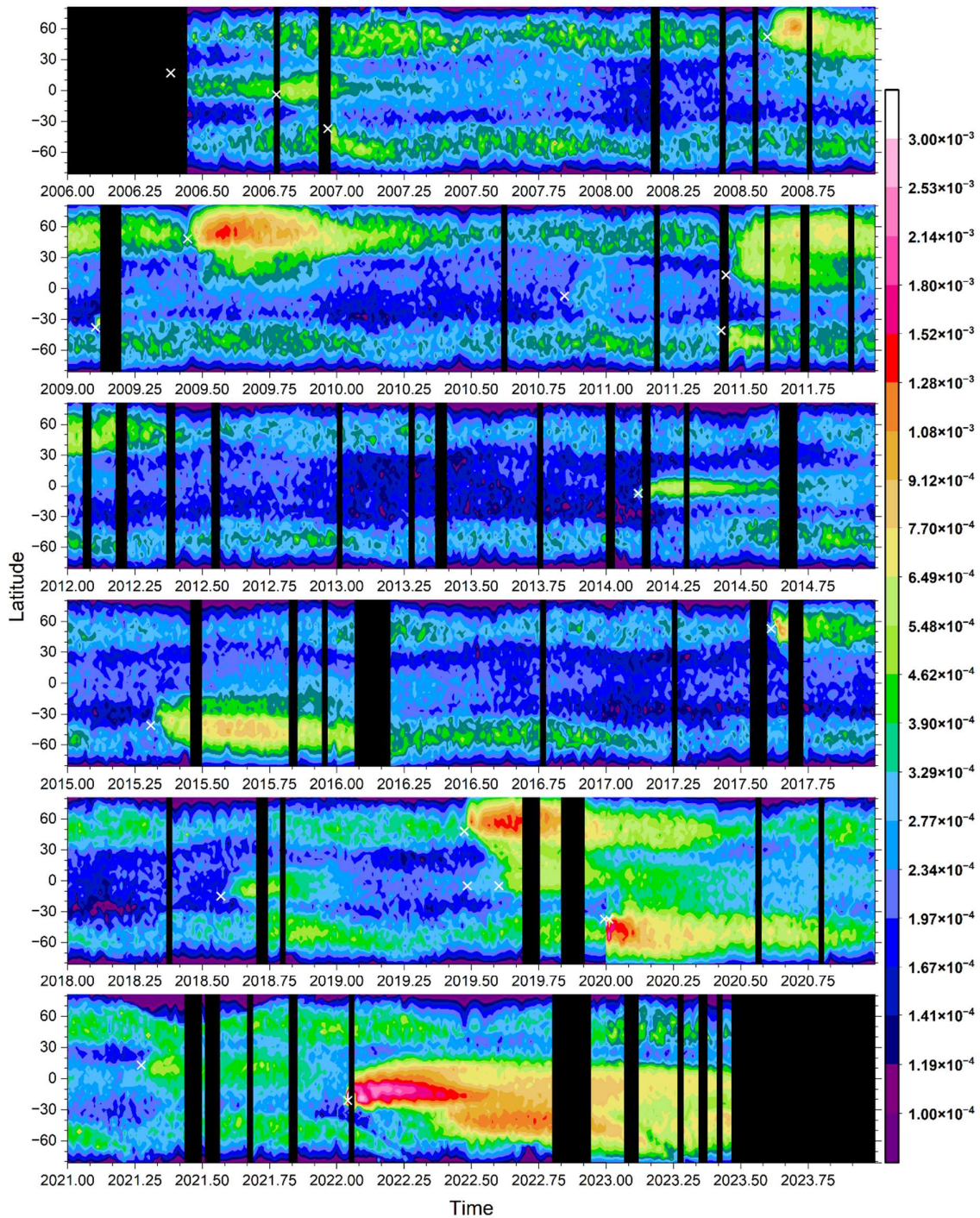
282

283 Raikoke eruption (Figure 2h) and the Australian wildfire in the last days of 2019 (Figure  
284 2i). Also, the 2011 Nabro eruption (Figure 2d) tends to deviate from the commonly  
285 adopted lidar ratio of 50 sr of stratospheric aerosol, however the observations are too  
286 few for a firm conclusion. In the forthcoming presentation the lidar ratio of 50 sr will be  
287 used before the influence from deviations is addressed in sections 3.4 and 3.5.

### 288 **3.2 Stratospheric aerosol events overview**

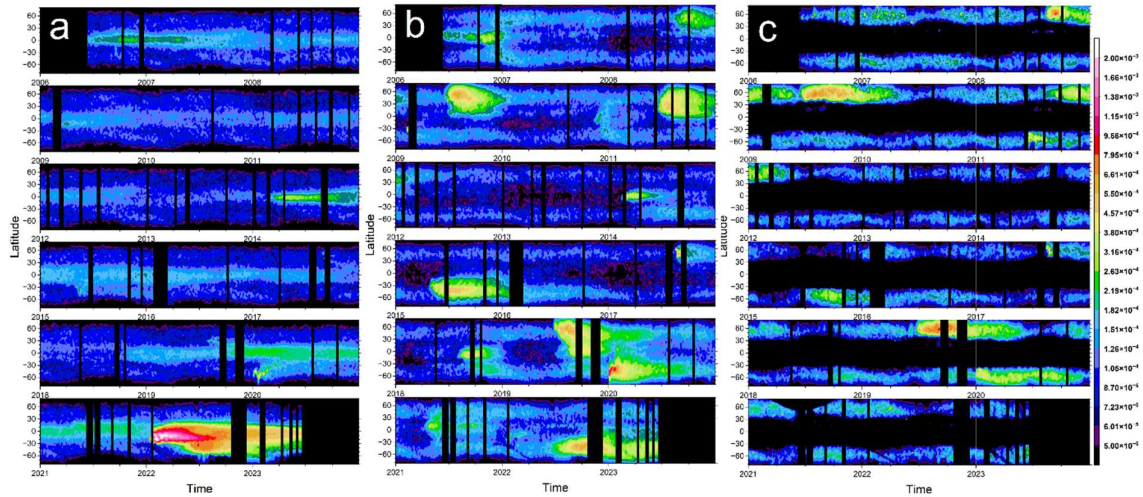
289 At least 15 volcanic eruptions and 5 wildfires clearly affected the stratospheric aerosol  
290 in the CALIOP era (Table 1). The latitude distribution of the stratospheric aerosol from  
291 the tropopause to 35 km altitude is shown in Figure 3, and subdivided into three layers,  
292 dBD, sBD, and LMS, in Figure 4 with full size versions in supplementary Figures S1 – S3.  
293 Additionally, the altitude distribution is shown in three latitude ranges (-80 to -20°, -20 to  
294 20° and 20 to 80°) in Figure 5 (supplementary Figures S4 – S6).

295 The influence from injections of aerosol from volcanic eruptions and wildfires has  
296 durations of a few months to several years (Friberg et al., 2018). The latter category is  
297 the aerosol events that enter the dBD branch in the tropics. The outstanding event  
298 fulfilling this requirement in the period studied is the submarine eruption of Hunga  
299 Ha’apai in 2022 (Figures 4a and 5a, b) where intense volcanism – sea interaction  
300 (Seabrook et al., 2023; Mastin et al., 2024) formed large quantities of stratospheric  
301 aerosol, whereas aerosol formation from SO<sub>2</sub> could explain only ~30% of the AOD  
302 (Martinsson et al., 2025). The remaining aerosol events in the dBD have much lower  
303 AODs. The Kelut eruption in 2014 affected the dBD for approximately 4 years. The  
304 combined effect of the 2006 eruptions of Soufriere Hills and Rabaul (Figure 5b) show  
305 similar long-term effects on the dBD in the tropics (Figure 4a). The combined effects of  
306 4 volcanic eruptions, the 2018 Ambae, the two 2019 Ulawun and the 2021 Soufriere  
307 eruptions, gradually increased the dBD aerosol load in the tropics. In addition to these  
308 tropical eruptions, some extratropical aerosol events affected the dBD: the 2015  
309 Calbuco eruption and some plumes injected above the main aerosol layer of the 2019  
310 Raikoke eruption. Three wildfires also contributed aerosol to the extratropical dBD, the  
311 2009 Australian, the 2017 Canada/USA and the 2019 Australian wildfires. The aerosol  
312 from the latter fire formed a vortex where



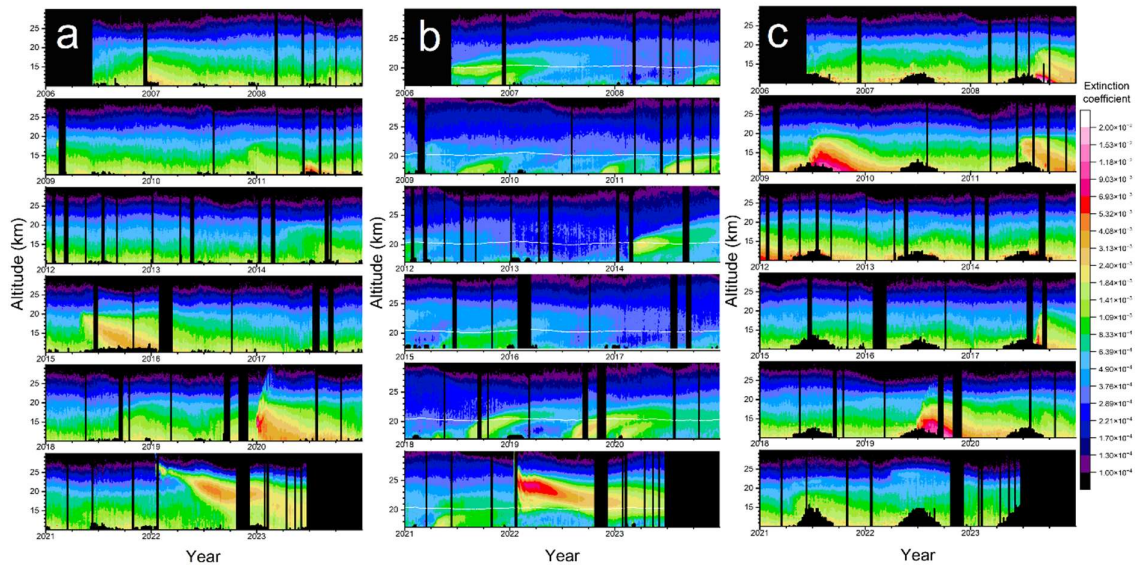
313

314 **Figure 3.** AOD integrated from the tropopause to 35 km altitude averaged over 4 days  
 315 and 3 degrees in latitude. The lidar ratio is set to 50 sr. Color scale: The data is latitude  
 316 weighted in the way that the global AOD contribution per degree of latitude is shown, i.e.  
 317 the sum over latitude is the total AOD at any given time. The data has been extrapolated  
 318 at high latitudes as described in section 2.1, Figure S7 shows the data without  
 319 extrapolation. White crosses indicate time and latitude of aerosol events mentioned in  
 320 Table 1.



321

322 Figure 4. AOD integrated in three layers: a) dBD, b) sBD and c) LMS. The color scale is  
 323 latitude weighted as explained in the caption of Figure 3. Full size images are displayed  
 324 in the Supplementary material, Figures S1 – S3.



325

326 Figure 5. Extinction coefficients ( $\text{km}^{-1}$ ) averaged in three latitude bands: a) southern  
 327 extratropics ( $-80$  to  $-20^\circ$ ), b) tropics ( $-20$  to  $20^\circ$ ) and c) northern extratropics ( $20$  to  $80^\circ$ ).  
 328 Full size images are displayed in the Supplementary material, Figures S4 – S6.

329

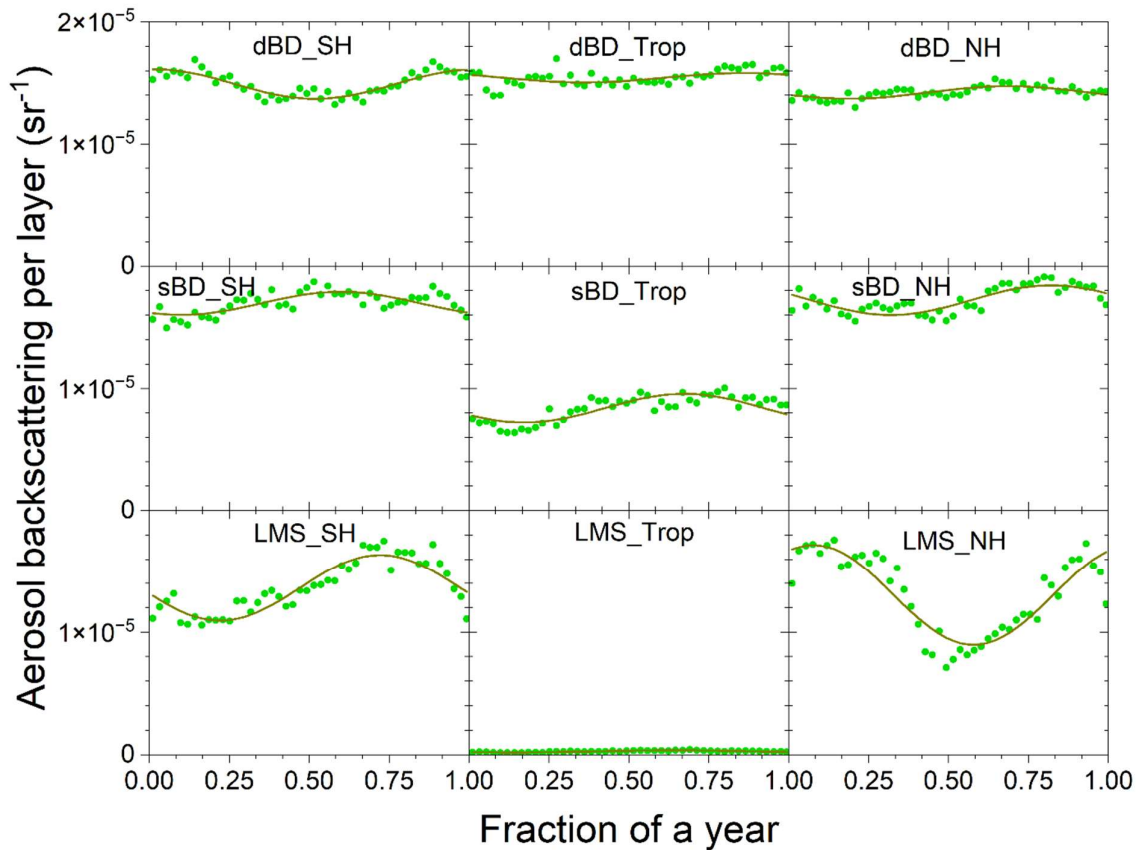
330 the aerosol rose above 31 km altitude (Kablick et al., 2020). The extratropical aerosol  
 331 events leave the dBD faster than the tropical ones because of the extratropical  
 332 downward motion of the BD circulation.

333 The shallow Brewer-Dobson (sBD) branch (Figure 4b) displays no such strong aerosol  
334 event as the effect of the 2022 Hunga Ha’apai eruption on the dBD (Figure 4a). On the  
335 other hand, many events had intermediate or small impacts. The Australian wildfires at  
336 the end of 2019 and the beginning of 2020 made an initial strong impact that was rapidly  
337 reduced by loss of 90% of the aerosol with a half-life of 10 days, likely due to photolysis  
338 of organic aerosol (Friberg et al., 2023), as did the 2017 North American wildfire but with  
339 a lower aerosol load (Martinsson et al. 2022) and, to a still lower extent, the 2009  
340 Australian wildfire. The main volcanic eruptions affecting the sBD branch were the 2008  
341 Kasatochi, 2009 Sarychev, 2011 Nabro, 2015 Calbuco, 2019 Raikoke and, after a delay  
342 due to transport from the dBD branch, the 2022 Hunga Ha’apai eruptions (Figure 4a, b).  
343 Other volcanos with smaller impact on the sBD branch were the 2006 Soufriere Hills  
344 and Rabaul, the 2010 Merapi, 2014 Kelut, 2018 Ambae, 2019 Ulawun (2 eruptions) and  
345 2021 Soufriere eruptions.

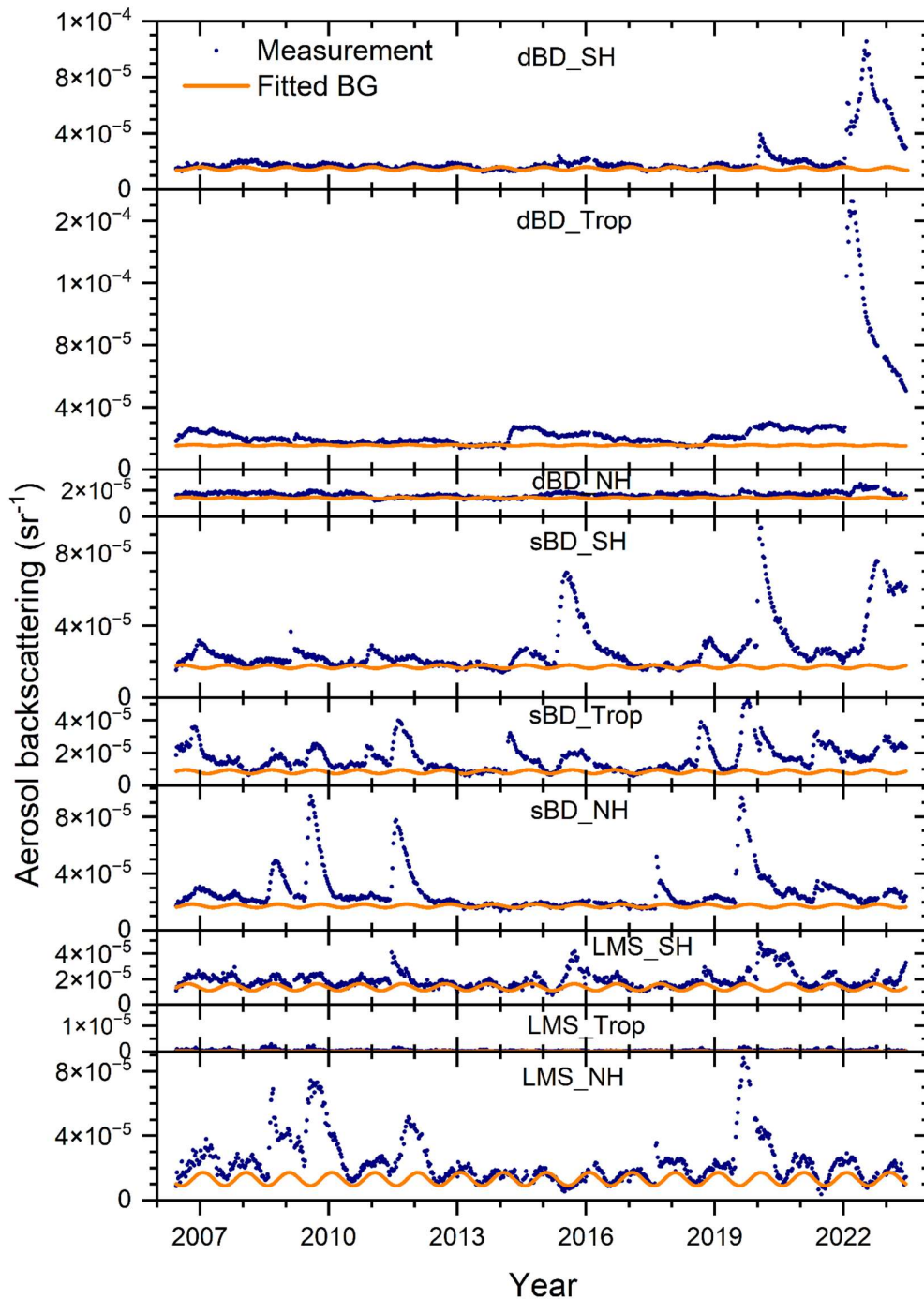
346 The LMS (Figure 4c), the last stratospheric part passed by the air and its trace  
347 substances in the large-scale stratospheric circulation before exiting to the  
348 troposphere, is affected by all stratospheric aerosol events. In addition, some  
349 extratropical aerosol events do not reach beyond the LMS. The Kasatochi eruption  
350 resulted in two distinct aerosol layers, a thin layer in the sBD whereas the main part of  
351 its effluents was injected both sides of and close to the tropopause (Andersson et al.,  
352 2015). Other exclusive LMS events in the period studied here are the 2011 Puyehue-  
353 Cordón Caulle eruption and the 2006 Australia wildfire.

354 Most volcanic eruptions show a gradual increase in AOD over few months before  
355 reaching its maximum because of the time required for aerosol dynamical processing  
356 and to transform sulfur dioxide into sulfate, which usually is the main component of the  
357 aerosol from volcanic eruptions. Notable exceptions are the 2022 Hunga Ha’apai and  
358 the 2011 Puyehue-Cordón Caulle eruptions (Figure 3). The aerosol of the latter eruption  
359 mainly consisted of volcanic ash (Vernier et al., 2013) and the former by aerosol  
360 containing sulfate and sea-salt from volcanism – sea interaction (Martinsson et al.,  
361 2025). These eruptions are thus less influenced by delay in aerosol formation from  
362 chemical transformation. The wildfires in the years 2009, 2017, 2019 and 2020 also

363 rapidly reach the maximum AOD before a decline due to photolysis of organic  
 364 compounds reduces the AOD by 90% (Martinsson et al., 2022; Friberg et al., 2023).



365  
 366 **Figure 6.** Average backscattering, which when multiplied with the lidar ratio becomes  
 367 the AOD of the layer, of the background aerosol extracted based on the three lowest  
 368 average values of each 8-day period over the year in the CALIOP era (2006 – 2023). The  
 369 extracted data were fitted to a constant and a sinusoidal function. (Exceptions: the two  
 370 lowest 8-day averages were used for “dBD\_Trop” and “sBD\_Trop” due to infrequent  
 371 background values.) The extraction was undertaken in nine regions spanned by  
 372 latitudes: -80 to -20° (SH), -20 to 20° (Tropics), 20 to 80° (NH) and altitude ranges: the  
 373 tropopause to 380 K isentrope (LMS), 380 to 470 K isentrope (sBD), 470 K to 35 km  
 374 altitude (dBD). The data were latitude weighted in the way that the sum of the nine  
 375 layers is the global aerosol backscattering.



376

377 **Figure 7.** Stratospheric aerosol average backscattering, which when multiplied with the  
 378 lidar ratio becomes the AOD, and fitted background in nine latitude and altitude regions:  
 379 the deep BD branch (470 K isentrope to 35 km altitude), the shallow BD branch  
 380 (between isentropes 380 and 470 K) and the LMS (from the tropopause to the 380 K  
 381 isentrope) and three latitude regions the southern hemisphere extratropics (-80 to -20°),  
 382 the tropics (-20 to 20°) and the northern hemisphere extratropics (20 to 80°) to find time-  
 383 sections not or weakly affected by stratospheric aerosol events (see Fig. 4 and text for  
 384 details).

385

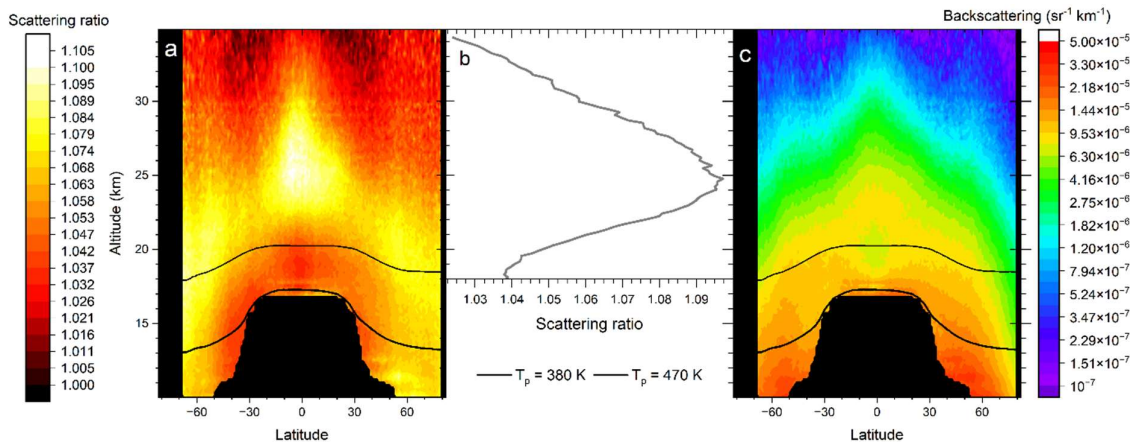
### 386 **3.3 Stratospheric background**

387 The stratospheric background aerosol is not a well-defined concept. One way is to  
388 include all but major aerosol events in the background to obtain a persistently variable  
389 background (Solomon et al., 2011). An alternative background is based on SAGE II  
390 measurements in the volcanically quiescent period in the late 1990s to early 2000s  
391 (Kremser et al., 2016). CALIOP measurements were not available in those years. A  
392 volcanic eruption or wildfire rarely affects the entire stratosphere. Therefore, we divided  
393 the stratosphere into nine sections by altitude and latitude thereby increasing the  
394 probability of finding conditions close to background separately in each of the layers  
395 using the average of the three lowest average backscattering values (in two cases the  
396 two lowest) of each layer over the year (Figure 6), as described in the methods section.

397 The distribution of aerosol over the nine layers used to extract the background aerosol is  
398 shown in Table 2. Seven of the nine layers each contain 11 – 15% of the background  
399 aerosol in the stratosphere from the tropopause to 35 km altitude during conditions that  
400 are close to background. The smallest contribution comes from the tropical LMS, which  
401 is to be expected given the small air volume of that layer. The tropical sBD also has a  
402 small contribution, but that cannot be explained by the air volume. This layer where  
403 tropospheric air enters the stratosphere extends to approximately 20 km altitude, where  
404 UV radiation intensity is too weak to efficiently oxidize carbonyl sulfide (Weisenstein et  
405 al., 1997), which is an important precursor gas of the stratospheric background aerosol  
406 (Crutzen, 1976; Kremser et al., 2016), a topic we return to below. Seasonal changes in  
407 aerosol background average backscattering are most pronounced in the extratropical  
408 LMS, especially in the NH. The volume of LMS varies over the year. That variation  
409 (Appenzeller et al., 1996) approximately coincides with the variation in Figure 6 both in  
410 terms of seasonality and the stronger amplitude in the LMS of the NH. The seasonal  
411 variation of background backscattering in the LMS therefore likely reflects both the seasonal  
412 variation of LMS volume and true variability in aerosol loading. Poleward transport in the BD  
413 circulation maximizes in the winter resulting in increased extratropical downward  
414 motion of the stratospheric aerosol layer in the spring resulting in low aerosol load in the  
415 summer LMS when the mass transport across its upper boundary is at its minimum. The

416 latter also coincides with the weakening of the subtropical Jetstream which increases  
 417 the tropospheric influence on the LMS. In the summer/early fall there is also influence  
 418 from ATAL (Vernier et al., 2015) and small wildfires briefly affecting the stratosphere  
 419 (Peterson et al., 2025). The chemical composition of the LMS aerosol of the Northern  
 420 hemisphere in that period differs from winter/spring/early summer by having a larger  
 421 carbon than sulfur content (Martinsson et al., 2019). The change in composition can be  
 422 caused by the ATAL and/or small wildfires which thus contribute to the effect of the  
 423 large-scale stratospheric circulation in the build-up of the NH LMS aerosol load during  
 424 late summer and fall.

425 The average backscattering of the stratospheric aerosol and the estimated background  
 426 (Figure 6) in nine altitude and latitude layers is shown in Figure 7. By comparing these  
 427 two quantities, we verify the underlying assumption in the method used to obtain the  
 428 background that the stratospheric aerosol background has no long-term trend, which  
 429 agrees with previous observations (Kremser et al., 2016). Subtracting the background,



430

431 **Figure 8.** The stratospheric aerosol averaged over year 2013, which was close to  
 432 background conditions. a) The scattering ratio, i.e., the ratio between the total to the  
 433 modeled backscattering of air molecules. This intensive parameter is not latitude  
 434 weighted. b) Average scattering ratio in the central tropics (latitudes  $-10$  to  $10^\circ$ )  
 435 dependence on altitude. c) Average aerosol backscattering, this extensive quantity is  
 436 latitude weighted. Black lines in a) and c) are the yearly average positions of the  
 437 potential temperatures ( $T_p$ ) 380 and 470 K.

438

439 we obtain the average backscattering from volcanic eruptions and wildfires. The net  
 440 average backscattering of the layers was converted to AOD of the layers by  
 441 multiplication with the lidar ratio of 50 sr in Figure S8 with contributions from volcanic  
 442 eruptions and wildfires as described in section 3.2.

443 Except for a tiny peak in the LMS in the Northern extratropics, 2013 is close to  
 444 background conditions (Figure 7). The stratospheric background aerosol is often  
 445 thought of as a layer located above 20 km altitude in the tropics and lower in the  
 446 extratropics. This is approximately true in terms of scattering ratio (R), the optical  
 447 equivalent of mixing ratio (Figure 8a). More than half of the air entering the tropical  
 448 stratosphere is transported polewards in the sBD (Lin and Fu, 2013), where the  
 449 scattering ratio remains low in a band closest to the tropopause (Figure 8a). This band  
 450 contains young stratospheric air compared to air at the same altitude but at higher  
 451 latitude (Austin and Li, 2006; Butchart, 2014; Ploeger et al., 2021). In the air rising  
 452 further in the tropical stratosphere a dramatic increase of the aerosol mixing ratio can  
 453 be seen above 20 km altitude. The aerosol signal increases by a factor 2.5 (Figure 8b)  
 454 from 19 to 25 km altitude in the latitude range -10 to 10°, i.e., 70% of the aerosol at 25  
 455 km is formed above 19 km altitude. The dBD air is transported polewards and descends  
 456 at higher latitudes than the sBD air (Figure 8a). With a typical vertical

457 **Table 2.** Average backscattering of background aerosol and AOD of aerosol events in  
 458 2006 - 2023 and the distribution over nine stratospheric layers.

Backscattering background <sup>a</sup>				
	<i>Global</i>	SH	Tropics	NH
<i>Total</i>		40%	21%	39%
dBD	39%	13%	14%	12%
sBD	37%	15%	7.3%	15%
LMS	24%	12%	0.2%	11%
AOD aerosol events <sup>b</sup>				
	<i>Global</i>	SH	Tropics	NH
<i>Total</i>		33%	31%	35%
dBD	31%	9.0%	18%	4.0%
sBD	43%	15%	13%	15%
LMS	26%	9.0%	0.4%	17%

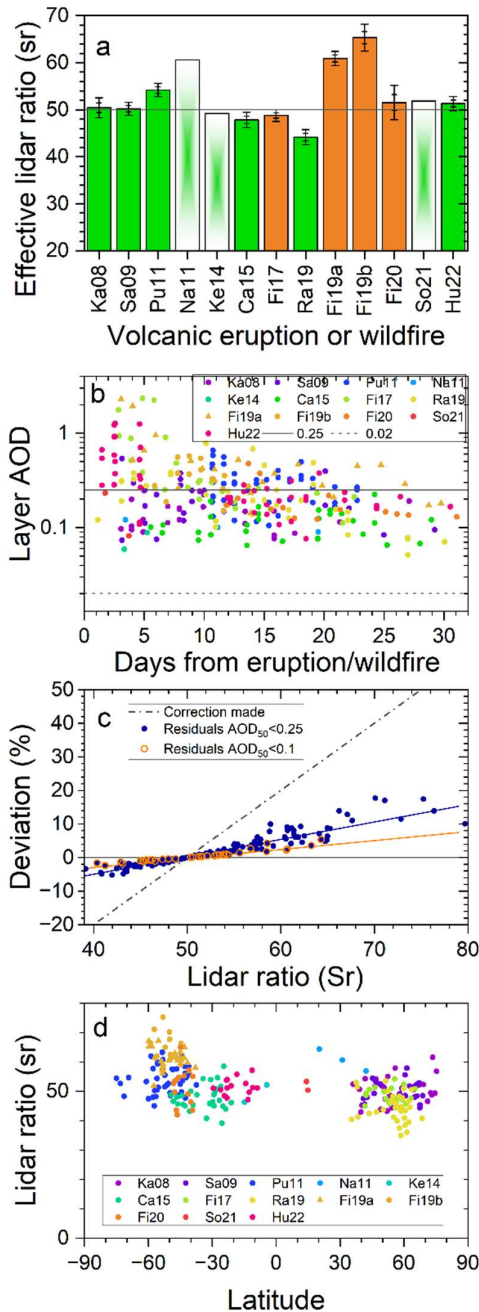
459 <sup>a</sup>Average backscattering of background = 0.00011 sr<sup>-1</sup>

460 <sup>b</sup>Average AOD from aerosol events (2006 – 2023) = 0.0031

461

462 velocity of 20 m/day (Mote et al., 1998) the transport from the tropical tropopause (at 17  
463 km) to 19 km altitude requires approximately 100 days, providing ample time for  
464 conversion of SO<sub>2</sub> before reaching the latter altitude (Nicknisch et al., 2025). Hence, little  
465 SO<sub>2</sub> enters the dBD, implying particle formation from another source. Intensifying UV  
466 radiation with altitude causes oxidation of the most abundant sulfur compound in the  
467 atmosphere, i.e., carbonyl sulfide (OCS) (Crutzen, 1976; Kremser et al., 2016), whereas  
468 this compound remains intact in the sBD. The requirement of intense UV radiation for  
469 oxidation makes OCS an important aerosol formation pathway mainly in the dBD. The  
470 formed aerosol is transported polewards where downward transport brings the aerosol  
471 to the sBD and LMS layers before the transport out of the stratosphere (Figure 8a). The  
472 formation pathways of the stratospheric background aerosol are still debated. The  
473 estimated contribution of OCS to the stratospheric background aerosol ranges from 20  
474 – 50% (Sheng et al., 2015; Chin and Davies, 1995) to 70% or more (Crutzen, 1976; Brühl  
475 et al., 2012). High-resolution lidar data, like that of CALIOP, can be used to constrain  
476 modeling efforts to quantify sulfurous aerosol sources by reconstructing the CALIOP  
477 observations in Figure 8 to understand the sources of the background aerosol.

478 When instead considering the absolute background aerosol load (Figure 8c) we find the  
479 highest aerosol load at low stratospheric altitudes. The air in the Brewer-Dobson



480

481 **Figure9.** a) Average lidar ratios according to Fig. 2 with standard errors and 95% ranges  
 482 of volcanic eruptions and wildfires. Too few observations for error estimations were  
 483 obtained for the eruptions of Nabro (Na11), Kelut (Ke14) and Soufriere (So21). b) AODs  
 484 of aerosol layers with  $dS/dR \times \sigma(R) < 10$  sr Vs. time from the eruption or wildfire. The full  
 485 line illustrates approximate maximum layer AOD after 1 month, and the broken line  
 486 indicates the approximate maximum layer AOD observable by limb-viewing techniques  
 487 (note: logarithmic y-scale). c) Correction of AOD obtained by setting the lidar ratio to 50  
 488 sr ( $AOD_{50}$ ), based on a linear dependence of the AOD on the lidar ratio. The residual  
 489 deviation after the correction of two categories is also shown: aerosol layers with  $AOD_{50}$   
 490  $< 0.1$  and  $< 0.25$ . d) Estimated lidar ratios in Figure 2 Vs. latitude.

491 circulation becomes compressed during the downwelling in the extratropics in  
492 accordance with the altitude-dependence of the atmospheric pressure. Mixing across  
493 the extratropical tropopause culminating in the late summer with the ATAL affects the  
494 aerosol load in the LMS but does not affect the mixing ratios appreciably (Figure 8a).  
495 However, somewhat higher scattering ratios are found in the ATAL region (15 – 45° N and  
496 13 – 18 km altitude (Vernier et al., 2015)) compared with the same region of the  
497 southern hemisphere. In monthly resolution, rather than the yearly resolution of Figure  
498 8, enhanced aerosol load in the ATAL area is clearly visible in July – September 2013  
499 (Martinsson et al., 2017). During background conditions approximately 60% of the  
500 aerosol backscattering signal (AOD divided by the lidar ratio) is found in the two lower  
501 layers, sBD and LMS (Table 2), containing aerosol transported from both the sBD and  
502 dBD of the tropics.

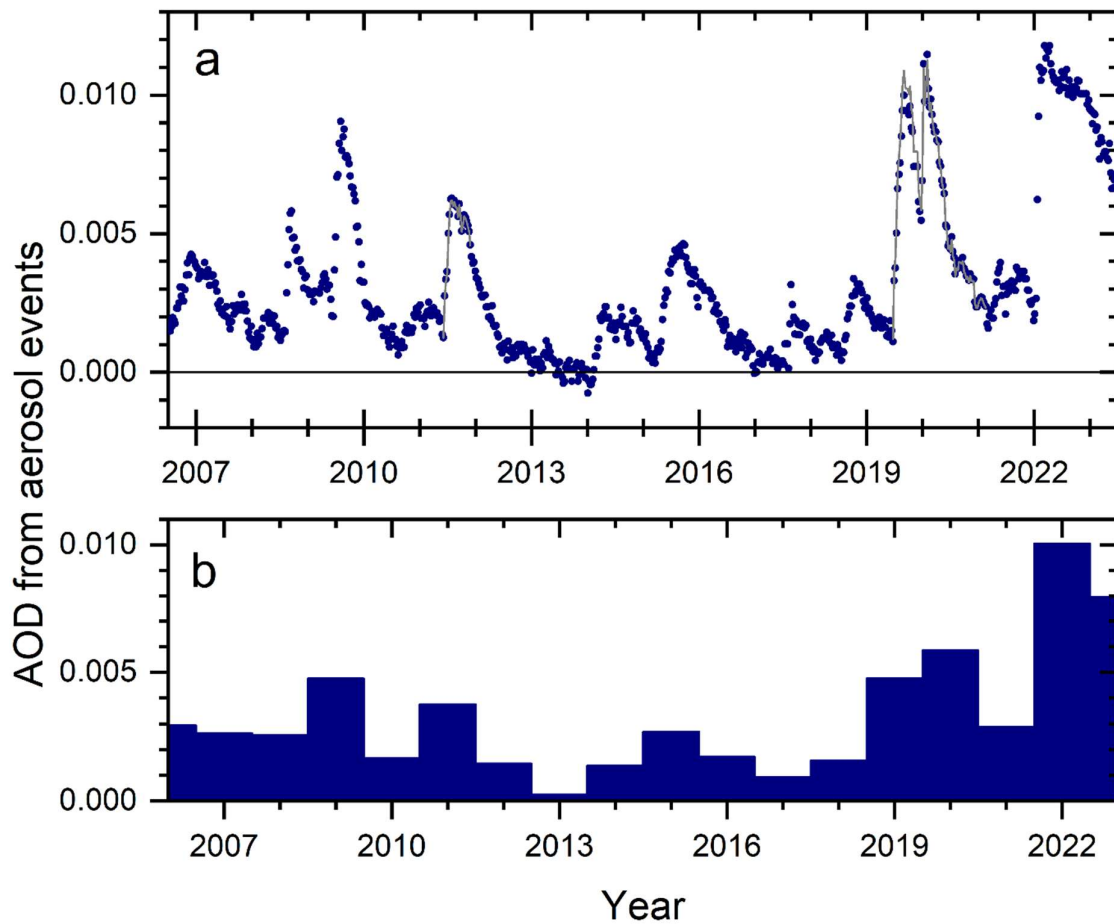
### 503 **3.4 Correction of lidar ratio**

504 Thus far we have presented AODs with the lidar ratio set to 50 sr. The lidar ratios of the  
505 individual measurements are shown in Figure 2. In Figure 9a we show the averages with  
506 statistical uncertainty (standard error and double-sided 95% confidence interval). As  
507 already pointed out, three of the eruptions (Nabro 2011, Kelut 2014 and Soufriere 2021)  
508 cannot be evaluated statistically due to few available measurements. Most of the  
509 aerosol events show effective lidar ratios of approximately 50 sr, whereas the aerosol  
510 from Puyehue-Cordón Caulle (2011), Raikoke (2019) and the Australian wildfires in the  
511 end of 2019 deviates from 50 sr by more than 5%.

512 To convert the AOD obtained using  $S_0 = 50$  sr to the estimated lidar ratio ( $S$ ) we need to  
513 consider the linear dependence of the AOD on the lidar ratio. A secondary effect relates  
514 to the level of AOD. For the latter, we need to evaluate the occurrence of dense aerosol  
515 layers. All the measurements fulfilling the criteria on uncertainty of the lidar ratio  
516 estimate (Figure 1) are displayed in Figure 9b. Initially layer AODs sometimes exceed 1.  
517 After 20 days the AOD of the individual aerosol layers is mostly 0.25 and lower, except  
518 for the 2019 Australian wildfire that remain somewhat higher probably due to less air  
519 mixing in the vortex formed (Kablick et al., 2020). We corrected the AODs by  $S/S_0$  for  
520 volcanic eruptions and wildfires that formed an aerosol with effective lidar ratio  
521 deviating more than 5% from  $S_0 = 50$  sr, whereas the residual correction connected with

522 the AOD of an aerosol layer was not accounted for (see the methods section for further  
 523 detail) because the effect is small (Figure 9c). In the general evaluation we did not  
 524 separate the aerosol backscattering from the 2019 and 2020 Australian wildfires that  
 525 were only a few days apart. The 2020 fire was dominant in terms of AOD with 80 – 90%  
 526 of the total AOD from the two fires (Friberg et al., 2023). Here, we weigh the lidar ratios  
 527 of the two fires accordingly to obtain  $S = 53.3$  representing both fires.

528



529

530 **Figure 10.** Background-subtracted AOD of the stratosphere from the tropopause to 35  
 531 km altitude and averaged from  $-80$  to  $80^\circ$  in latitude. a) AOD from main stratospheric  
 532 aerosol events caused by volcanic eruptions and wildfires.  $AOD_{50}$  is shown (full grey  
 533 line) where correction due to lidar ratio deviating from 50 sr is undertaken (Pu11, Ra19  
 534 and Fi19&20). b) Yearly averages of data in a). Note that the horizontal tick marks  
 535 indicate start of a year in a) and the middle of a year in b). Also note that the averages of  
 536 years 2006 and 2023 span only half years due to the mid-year start (2006) and finish  
 537 (2023) of the CALIOP measurements.

538

539 The blue dots in Figure 10a over the stratospheric AOD were corrected for deviant lidar  
540 ratios in 2011 (Puyehue-Cordón Caulle eruption by +8%) and 2019 – 2020 (Raikoke  
541 eruption by -12% and Australian wildfires by +7%). The corresponding AOD using  $S_0 = 50$   
542 sr is represented by a thin gray line showing that the AOD was practically not affected by  
543 the correction in 2011 because that year was dominated by aerosol from another  
544 eruption (Nabro, Figure 3). The AOD from the Raikoke (2019) eruption shifted down  
545 slightly by the correction, and that of the 2019 – 2020 Australian wildfires shifted  
546 upwards.

547 Altogether the changes in AOD from the corrections due to deviant lidar ratio were  
548 found to be minor, the largest correction (-12%) was applied to the AOD of the Raikoke  
549 eruption. However, we could not statistically quantify all major aerosol events, most  
550 notably the Nabro eruption in 2011 (Figure 2). Our results show that assumption of an  
551 effective lidar ratio of 50 sr works satisfactory in most cases in the 17-year period  
552 studied when the stratospheric aerosol is influenced by volcanism or wildfires. The  
553 applied method to obtain the effective lidar ratio cannot be used for optically thin layers  
554 like the background aerosol.

### 555 **3.5 AOD of stratospheric aerosol events**

556 The AOD from aerosol events were approximately evenly distributed over the three  
557 latitude regions (-80 to -20°, -20 to 20° and 20 to 80°) studied (Table 2). The altitude  
558 distribution showed most influence from volcanic eruptions and wildfires in the sBD  
559 (43%), followed by the dBD (31%), and the often overlooked LMS (Andersson et al.,  
560 2015) held 26% of the AOD from aerosol events in the period 2006 – 2023.

561 The average stratospheric AOD, with the contribution from background aerosol  
562 subtracted, from the tropopause to 35 km altitude in the latitude range -80 to 80° is  
563 shown in Figure 10a. The intense volcanism – sea interaction of the Hunga Ha’apai  
564 eruption in the beginning of 2022 (Martinsson et al., 2025) resulted in the highest and  
565 broadest AOD peak (Figure 10a). Other prominent events were the Australian wildfires  
566 at the end of 2019 and the beginning of 2020, the eruptions of Raikoke (2019), Sarychev  
567 (2009), Nabro (2011), Calbuco (2015) and Kasatochi (2008) affecting the stratospheric

568 AOD together with several eruptions and wildfires having smaller contributions (Table  
569 1).

570 The average influence of volcanic eruptions and wildfires each year is shown in Figure  
571 10b. The most affected year was 2022 with an average AOD of 0.01 from aerosol events.  
572 That year is likely followed by 2023, for which we have no data from the second half of  
573 the year. Both these years were mainly affected by the 2022 Hunga Ha'apai eruption.  
574 Then follows 2020 (mainly the 2019-20 Australian wildfires with some contribution from  
575 the Raikoke eruption) with background-subtracted AOD of 0.006, 2009 (Sarychev) and  
576 2019 (Raikoke) both years with AOD of 0.005, whereas 2011 (mainly Nabro) reach AOD  
577 from aerosol events of almost 0.004. The average background-subtracted AOD from  
578 volcanic eruptions and wildfires from 2006 to 2023 is 0.0031. The background aerosol  
579 produces global average backscattering of  $0.00011 \text{ sr}^{-1}$ , which, with the commonly used  
580 assumption of a lidar ratio of 50 sr, corresponds to a stratospheric background AOD of  
581 0.0057.

582 The yearly average AOD from aerosol events ranges from 0.0002 (in 2013) to 0.010  
583 (2022) and the average over the 17 years studied is 0.0031. Making use of previous  
584 estimates of the relation between radiative forcing (F) and stratospheric AOD ( $F = -$   
585  $24 \times \text{AOD}$  in  $\text{W/m}^2$ ) (Schmidt et al., 2018), we can obtain a first, simplified estimate of the  
586 radiative effect of the stratospheric aerosol events. This relation is based on volcanic  
587 sulfate aerosol, which is the dominant type of stratospheric aerosol event in the 17-year  
588 period studied. The relation is not designed to deal with absorbing wildfire aerosol,  
589 which cause uncertainty in the average radiative forcing of the period estimated here.  
590 This simplified, order-of-magnitude estimate of the global stratospheric yearly average  
591 total effective radiative forcing due to volcanic eruptions and wildfires varies between -  
592  $0.006$  and  $-0.24 \text{ W/m}^2$ , with the average  $-0.074 \text{ W/m}^2$  in the period 2006 to 2023.  
593 Assuming a lidar ratio of 50 sr, the stratospheric background aerosol effective radiative  
594 forcing becomes  $-0.14 \text{ W/m}^2$ .

#### 595 **4. Discussion**

596 Stratospheric aerosol optical properties are often described using solar occultation  
597 data, especially from the 22 years of SAGE II measurements (Bauman et al., 2003;  
598 Thomason et al., 2018). Prior comparisons of CALIOP lidar-based results with solar  
599 occultation (SAGE III/ISS) show agreement within approximately 10% in the latitude  
600 range -30 to 30° and increasing discrepancy at midlatitudes reaching above 50% at high  
601 latitudes for background aerosol in the altitude range 20 – 30 km (Kar et al., 2019), and  
602 discrepancies exceeding 50% is reported at altitudes below 17 km (Kovilakam et al.,  
603 2023). The main reason for these differences was attributed to the unknown lidar ratio  
604 of CALIOP (Kar et al., 2019; Kovilakam et al., 2023). Here we have estimated the CALIOP  
605 effective lidar ratio of the aerosol from several volcanic eruptions and wildfires (Figure  
606 2), and in Figure 9d the latitude distribution of the estimates is shown. Using the  
607 standard lidar ratio of 50 sr cannot explain the latitude- and altitude-dependence in the  
608 lidar – solar occultation comparison obtained in Kar et al. (2019) and Kovilakam et al.  
609 (2023) for aerosol from volcanic eruptions and wildfires in the CALIOP era.

610 The latitude-dependent discrepancy at 532 nm wavelength between SAGE III/ISS and  
611 CALIOP at high altitudes in the period June 2017 to August 2018 above 20 km (, i.e.,  
612 essentially in the dBD) reported by Kar et al. (2019) concerns a period when the dBD  
613 was close to background (Figure 7). The method used here for estimating the lidar ratio  
614 does not work for background conditions (Figure 1). Using the standard CALIOP lidar  
615 ratio for the background aerosol (50 sr) results in the global average background AOD of  
616 0.0057. SAGE II measurements during the volcanically quiescent period 1998 – 2000  
617 resulted in AOD of 0.0040 (estimated from Solomon et al. (2011), their Figure 2), who  
618 integrated the stratospheric AOD from 15 km altitude. When removing the stratospheric  
619 aerosol data below 15 km from the CALIOP measurements, the stratospheric  
620 background AOD is reduced by 31% to 0.0039 using lidar ratio 50 sr. This is almost  
621 identical to the background AOD reported in Solomon et al. (2011), thus indicating that  
622 the stratospheric background aerosol on average has a lidar ratio close to 50 sr. Kar et  
623 al. (2019) found that aerosol backscattering during background conditions at altitudes  
624 above 20 km in the extratropics should be converted to AOD by a variable lidar ratio.  
625 Mid- and high-latitude air in this altitude range has a high stratospheric age (~5 years)  
626 (Ploeger et al., 2021), implying that particle gravitational settling has long time to affect

627 the particle size distribution, and hence the optical properties of the aerosol. In Figure  
628 8c we find most of the aerosol above 20 km altitude to be located in the tropics,  
629 implying that the deviations at high latitudes that Kar et al. (2019) reported have little  
630 impact on global AOD, and thus little impact on our comparison with Solomon et al.  
631 (2011) that deals with the entire stratosphere above 15 km altitude.

632 In a comparison by Kovilakam et al. (2023) between CALIOP and SAGE III/ISS during  
633 November 2017, 2 – 3 months after the Canada/USA fire (Table 1) large deviations were  
634 found at high latitudes and altitudes as in Kar et al. (2019), as described above.  
635 Kovilakam et al. (2023) also found large differences in the densest part of the  
636 stratosphere, i.e., at altitudes below 17 km. In GloSSAC the more than 50% lower values  
637 of limb-viewing techniques (SAGE and OSIRIS) than CALIOP were adopted, justified by  
638 citing uncertainties in the lidar ratio to discard CALIOP results at low altitudes  
639 (Kovilakam et al., 2023).

640 The main advantages of solar occultation measurements are that extinction is  
641 measured and that several wavelengths are available. Lidar measurements also have  
642 some distinct advantages. Lidars with nadir view have several hundred kilometers  
643 shorter measurement path enabling measurements in dense aerosol layers (Martinsson  
644 et al., 2022, their Figure 7) producing viable, quantitative results when limb views fail,  
645 provided that the lidar ratio is known. The lidar vertical resolution is superior and is not  
646 relying on assumptions on homogeneity of the aerosol layer measured, like solar  
647 occultation measurements do (Damadeo et al., 2013). Accurate altitude descriptions  
648 with high vertical resolution of stratospheric injections (Sandvik et al., 2021) are vital for  
649 the outcome of stratospheric aerosol modeling (Axebrink et al., 2025). Relying on these  
650 points we argue that the role of lidar measurements should be re-evaluated. Existing  
651 methods differ in their sensitivity to aerosol properties and in their temporal coverage.  
652 We need to take advantage of the best qualities of all available methods, both in terms  
653 of physical properties and time coverage. Re-evaluation of CALIOP data could improve  
654 stratospheric aerosol climatologies, like GloSSAC (Thomason et al., 2018, Kovilakam et  
655 al., 2020; Kovilakam et al., 2023), that are designed for the modeling community,  
656 ultimately leading to a better representation of the stratospheric aerosol in climate  
657 modeling.

658 Hopefully the lidar ratio of stratospheric aerosol can be further clarified when the  
659 aerosol load is close to background conditions by lidar systems measuring both  
660 backscattering and extinction. The ATLID aboard the EarthCARE satellite (Illingworth et  
661 al., 2015) that started to produce data in July 2024 and the NASA and Italian Space  
662 Agency collaboration on the 3 wavelength lidar CALIGOLA planned for launch in the  
663 early 2030s (Behrenfeld et al., 2023) are future means to further clarify extinction  
664 obtained from lidars, and to optimally combine solar occultation and lidar  
665 measurements for future long-term records on the optical properties of the  
666 stratospheric aerosol with high and unambiguous vertical resolution.

## 667 **5. Conclusions**

668 The entire backscattering record at 532 nm wavelength of the satellite-based lidar  
669 system CALIOP spanning years 2006 to 2023 was investigated in this study. During this  
670 period injections of aerosol and precursor gases into the stratosphere of 15 volcanic  
671 eruptions and 5 wildfires were identified. The effective lidar ratios of 12 volcanic  
672 eruptions and wildfires were investigated to convert the measured backscattering to  
673 extinction. The measurements were evaluated and corrected for attenuation using the  
674 lidar ratio  $S_0 = 50$  sr. The aerosol events having a lidar ratio deviating by more than 5%  
675 from  $S_0$  were corrected after the general evaluation.

676 Background aerosol conditions are more likely to occur in sublayers than throughout  
677 the entire stratosphere. The stratosphere was therefore subdivided into 9 layers  
678 spanned by altitude (lowermost stratosphere (LMS), shallow Brewer-Dobson branch  
679 (sBD), deep Brewer-Dobson branch (dBD)) and latitude intervals (tropics and Southern  
680 and Northern extratropics). The estimated backgrounds of layers were combined to  
681 obtain the background aerosol of the entire stratosphere. The backscattering of  
682 background aerosol was converted to aerosol optical depth (AOD) using a lidar ratio of  
683 50 sr. That AOD agrees well with measurements with solar occultation (SAGE II) during  
684 1998 – 2000 in the volcanically quiescent period. The average backscattering of seven of  
685 the nine layers each contains 11 - 15% of the entire background aerosol. The tropical  
686 LMS has a small contribution due to very small volume compared to the other layers.  
687 The tropical sBD was also clearly lower (7%) because oxidation of carbonyl sulfide

688 (OCS) occurs at higher altitudes in the upwards moving air in the tropical stratosphere.  
689 We find that 70% of the aerosol in the tropical dBD is formed above 19 km altitude  
690 during background conditions, due to formation from OCS. A several kilometers thick  
691 band of low aerosol load directly above the tropopause was identified which we  
692 attribute to young stratospheric air transported in the sBD. Above that layer a broad  
693 band with high aerosol load was found which we identify as the tropical dBD air that is  
694 transported polewards and downwards resulting in high aerosol load in the sBD and  
695 LMS at mid and high latitudes. Considering the ongoing debate on the sources of  
696 stratospheric background aerosol, these highly resolved CALIOP data could be useful to  
697 constrain modeling efforts on the sources of the stratospheric sulfurous aerosol.

698 The background aerosol AOD (0.0057) was subtracted from the measurements to  
699 obtain the influence from aerosol and trace gas injections into the stratosphere. The  
700 most important aerosol events in the 17-year period are the 2022 Hunga Ha'apai  
701 eruption and the Australian wildfires (2019-20) followed by the volcanic eruptions  
702 Raikoke (2019), Sarychev (2009) and Nabro (2011). The global yearly average AOD  
703 increase from volcanic and wildfire injections spans 0 to 0.010.

704 Limb-viewing solar occultation measurements have some distinctive advantages in that  
705 much of the early measurements in the satellite era were undertaken with that method.  
706 They also deliver direct measurements of extinction, and at several wavelengths. Here,  
707 we have estimated the effective lidar ratio of the CALIOP measurements to obtain  
708 extinction from backscattering measurements. Lidars operating in nadir view, like  
709 CALIOP, have several hundred kilometers (or a factor of more than 100) shorter  
710 measurement path than limb-viewers, allowing measurements in dense aerosol layers  
711 where limb-viewers fail. Lidars have unambiguous and superior vertical resolution over  
712 other satellite instruments providing models with important input on aerosol and trace  
713 gas injections into the stratosphere. Newer lidars that measure extinction are launched,  
714 under construction and planned. Future work should better reconcile lidar and solar  
715 occultation records and exploit their complementary strengths. With known effective lidar  
716 ratios the relation between CALIOP and solar occultation measurements needs to be  
717 re-evaluated, especially in the dense stratospheric air located below 17 km altitude in  
718 long-term records over the optical properties of the stratospheric aerosol.

719 **References**

- 720 Andersson, S. M., Martinsson, B. G., Friberg, J., Brenninkmeijer, C. A. M., Rauthe-  
721 Schöch, A., Hermann, M., van Velthoven, P. F. J., and Zahn, A.: Composition and  
722 evolution of volcanic aerosol from eruptions of Kasatochi, Sarychev and  
723 Eyjafjallajökull in 2008–2010 based on CARIBIC observations, *Atmos. Chem.*  
724 *Phys.*, 13, 1781–1796, <https://doi.org/10.5194/acp-13-1781-2013>, 2013.
- 725 Andersson, S. M., Martinsson, B. G., Vernier, J.-P., Friberg, J., Brenninkmeijer, C. A. M.,  
726 Hermann, M., van Velthoven, P. F. J., and Zahn, A.: Significant radiative impact of  
727 volcanic aerosol in the lowermost stratosphere, *Nat. Commun.*, 6, 1–8,  
728 <https://doi.org/10.1038/ncomms8692>, 2015.
- 729 Appenzeller, C., Holton, J.R., and Rosenlov, K.H.: Seasonal variation of mass transport  
730 across the tropopause, *J. Geophys. Res.* 101, 15071-15078, 1996.
- 731 Austin, J., and Li, F.: On the relationship between the strength of the Brewer-Dobson  
732 circulation and the age of stratospheric air, *Geophys. Res. Lett.*, 33, L17807,  
733 [doi:10.1029/2006GL026867](https://doi.org/10.1029/2006GL026867), 2006.
- 734 Axebrink, E., Sporre, M.K., and Friberg, J.: Impact of SO<sub>2</sub> injection profiles on simulated  
735 volcanic forcing for the 2009 Sarychev eruptions– investigating the importance of  
736 using high-vertical-resolution methods when compiling SO<sub>2</sub> data, *Atmos. Chem.*  
737 *Phys.*, 25, 2047–2059, <https://doi.org/10.5194/acp-25-2047-2025>, 2025.
- 738 Baars, H., Ansmann, A., Ohneiser, K., Haarig, M., Engelmann, R., Althausen, D.,  
739 Hanssen, I., Gausa, M., Pietruczuk, A., Szkop, A., Stachlewska, I. S., Wang, D.,  
740 Reichardt, J., Skupin, A., Mattis, I., Trickl, T., Vogelmann, H., Navas-Guzmán, F.,  
741 Haeferle, A., Acheson, K., Ruth, A. A., Tatarov, B., Müller, D., Hu, Q., Podvin, T.,  
742 Goloub, P., Veselovskii, I., Pietras, C., Haeffelin, M., Fréville, P., Sicard, M.,  
743 Comerón, A., Fernández García, A. J., Molero Menéndez, F., Córdoba-Jabonero,  
744 C., Guerrero-Rascado, J. L., Alados-Arboledas, L., Bortoli, D., Costa, M. J.,  
745 Dionisi, D., Liberti, G. L., Wang, X., Sannino, A., Papagiannopoulou, N., Boselli,  
746 A., Mona, L., D’Amico, G., Romano, S., Perrone, M. R., Belegante, L., Nicolae, D.,  
747 Grigorov, I., Gialitaki, A., Amiridis, V., Souppion, O., Papayannis, A., Mamouri, R.-  
748 E., Nisantzi, A., Heese, B., Hofer, J., Schechner, Y. Y., Wandinger, U., and  
749 Pappalardo, G.: The unprecedented 2017–2018 stratospheric smoke event:  
750 decay phase and aerosol properties observed with the EARLINET, *Atmos. Chem.*  
751 *Phys.*, 19, 15183–15198, <https://doi.org/10.5194/acp-19-15183-2019>, 2019.
- 752 Bauman, J. J., Russell, P. B., Geller, M. A., and Hamill, P.: A stratospheric aerosol  
753 climatology from SAGE II and CLAES measurements: 2. Results and  
754 comparisons, 1984–1999, *J. Geophys. Res.*, 108, 4383,  
755 <https://doi.org/10.1029/2002JD002993>, 2003.
- 756 Behrenfeld, M.J., Lorenzoni, L., Hu, Y., Bissom, K.M., Hostetler, C.A., Di Girolamo, P.,  
757 Dionisi, D., Longo, F., and Zoffoli, S.: Satellite Lidar Measurements as a Critical

758 New Global Ocean Climate Record, *Remote Sens.* 15, 5567. [https://doi.org/](https://doi.org/10.3390/rs15235567)  
759 10.3390/rs15235567, 2023.

760 Brühl, C., Lelieveld, J., Crutzen, P.J., and Tost, H.: The role of carbonyl sulphide as a  
761 source of stratospheric sulphate aerosol and its impact on climate, *Atmos.*  
762 *Chem. Phys.*, 12, 1239–1253, [www.atmos-chem-phys.net/12/1239/2012/](http://www.atmos-chem-phys.net/12/1239/2012/)  
763 doi:10.5194/acp-12-1239-2012, 2012.

764 Butchart, N., The Brewer-Dobson circulation, *Rev. Geophys.*, 52, 157–184,  
765 doi:10.1002/2013RG000448, 2014.

766 Carn, S.A., Krueger, A.J., Krotkov, N.A., Yang, K., and Evans, K.: Tracking volcanic sulfur  
767 dioxide clouds for aviation hazard mitigation, *Nat Hazards*, 51, 325–343 DOI  
768 10.1007/s11069-008-9228-4, 2009.

769 Carn, S.A., and Prata, F.J., Satellite-based constraints on explosive SO<sub>2</sub> release from  
770 Soufrière Hills Volcano, Montserrat, *Geophys. Res. Lett.*, 37, 1-5, L00E22,  
771 doi:10.1029/2010GL044971, 2010.

772 Carn, S. A., Krotkov, N. A., Fisher, B. L., and Li, C.: Out of the blue: Volcanic SO<sub>2</sub>  
773 emissions during the 2021–2022 eruptions of Hunga Tonga– Hunga Ha’apai  
774 (Tonga), *Front. Earth Sci.*, 10, 976962,  
775 <https://doi.org/10.3389/feart.2022.976962>, 2022.

776 Chin, M., and Davies, D.D.: A reanalysis of carbonyl sulfide as a source of stratospheric  
777 background sulfur aerosol, *J. Geophys. Res.* 100, 8993-9005, 1995.

778 Clarisse, L., Hurtmans, D., Clerbaux, C., Hadji-Lazaro, J., Ngadi, Y., and Coheur, P.-F.:  
779 Retrieval of sulphur dioxide from the infrared atmospheric sounding  
780 interferometer (IASI), *Atmos. Meas. Tech.*, 5, 581–594,  
781 <https://doi.org/10.5194/amt-5-581-2012>, 2012.

782 Clarisse, L., Coheur, P.-F., Prata F., Hadji-Lazaro, J., Hurtmans, D., and Clerbaux, C.: A  
783 unified approach to infrared aerosol remote sensing and type specification,  
784 *Atmos.Chem.Phys.*,13,2195–2221, [www.atmos-chem-phys.net/13/2195/2013/](http://www.atmos-chem-phys.net/13/2195/2013/)  
785 doi:10.5194/acp-13-2195-2013, 2013.

786 Crutzen, P.J.: The possible importance of CSO for the sulfate layer of the stratosphere,  
787 *Geophys. Res. Lett.* 3, 73-76, 1976.

788 Cruz, M.G., Sullivan, A.L., Gould, J.S., Sims, N.C., Bannister, A.J., Hollis, J.J., and Hurley,  
789 R.J.: Anatomy of a catastrophic wildfire: The Black Saturday Kilmore East fire in  
790 Victoria, Australia, *Forest Ecol. Manag.* 284, 269-295, 2012.

791 Damadeo, R.P., Zawodny, J.M., Thomason, L.W., and Iyer, N.: SAGE version 7.0  
792 algorithm: application to SAGE II, *Atmos. Meas. Tech.*, 6, 3539–3561,  
793 [www.atmos-meas-tech.net/6/3539/2013/](http://www.atmos-meas-tech.net/6/3539/2013/), 2013.

794 Friberg, J., Martinsson, B. G., Andersson, S. M., Brenninkmeijer, C. A. M., Hermann, M.,  
795 Van Velthoven, P. F. J., and Zahn, A.: Sources of increase in lowermost

796 stratospheric sulphurous and carbonaceous aerosol background concentrations  
797 during 1999–2008 derived from CARIBIC flights, *Tellus B*, 66, 23428,  
798 <https://doi.org/10.3402/tellusb.v66.23428>, 2014.

799 Friberg, J., Martinsson, B. G., Andersson, S. M., and Sandvik, O. S.: Volcanic impact on  
800 the climate– the stratospheric aerosol load in the period 2006–2015, *Atmos.*  
801 *Chem. Phys.*, 18, 11149–11169, <https://doi.org/10.5194/acp-18-11149-2018>,  
802 2018.

803 Friberg, J., Martinsson, B. G., and Sporre, M. K.: Short- and long-term stratospheric  
804 impact of smoke from the 2019–2020 Australian wildfires, *Atmos. Chem. Phys.*,  
805 23, 12557–12570, <https://doi.org/10.5194/acp-23-12557-2023>, 2023.

806 Fromm, M., Lindsey, D. T., Servranckx, R., Yue, G., Trickl, T., Sica, R., Doucet, P., and  
807 Godin-Beekmann, S.: The untold story of pyrocumulonimbus, *B. Am. Meteorol.*  
808 *Soc.*, 91, 1193–1209, 2010.

809 Fromm, M., Kablick III, G. P., Peterson, D. A., Kahn, R. A., Flower, V. J. B., and Seftor, C. J.:  
810 Quantifying the source term and uniqueness of the August 12, 2017 Pacific  
811 Northwest pyroCb event, *J. Geophys. Res.*, 126, e2021JD034928,  
812 <https://doi.org/10.1029/2021JD034928>, 2021.

813 Garofalo, L. A., Levin, E. J. T., Campos, T., Kreidenweis, S. N., and Farmer, D. K.:  
814 Emission and evolution of submicron organic aerosol in smoke from wild fires in  
815 the western United States, *ACS Space Chem.*, 3, 1237–1247, 2019.

816 Gelaro, R., McCarty, W., Suarez, M. J., Todling, R., Moloud, A., Takacs, L., Randles, C. A.,  
817 Darmenov, A., Bosilovich, M. G., Reichle, R., Wargan, K., Coy, L., Cullather, R.,  
818 Draper, C., Akella, S., Buchard, V., Conaty, A., da Silva, A. M., Gu, W., Kim, G.-K.,  
819 Koster, R., Lucchesi, R., Merkova, D., Nielsen, J. E., Partyka, G., Pawson, S.,  
820 Putman, W., Rienecker, M., Schubert, S. D., Seinkiewicz, M., and Zhao, B.: The  
821 Modern-Era Retrospective Analysis for Research and Applications, Version 2  
822 (MERRA-2), *J. Clim.* 30, 5419–5454, 2017.

823 Haywood, J.M., Jones, A., Clarisse, L., Bourassa, A., Barnes, J., Telford, P., Bellouin, N.,  
824 Boucher, O., Agnew, P., Clerbaux, C., Coheur, P., Degenstein, D., and Braesicke,  
825 P.: Observations of the eruption of the Sarychev volcano and simulations using  
826 the HadGEM2 climate model, *J. Geophys. Res.*, 115, D21212,  
827 [doi:10.1029/2010JD014447](https://doi.org/10.1029/2010JD014447), 2010.

828 Illingworth, A. J., Barker, H. W., Beljaars, A., Ceccaldi, M., Chepfer, H., Clerbaux, N.,  
829 Cole, J., Delanoë, J., Domenech, C., Donovan, D. P., Fukuda, S., Hirakata, M.,  
830 Hogan, R. J., Huenerbein, A., Kollias, P., Kubota, T., Nakajima, T., Nakajima, T. Y.,  
831 Nishizawa, T., Ohno, Y., Okamoto, H., Oki, R., Sato, K., Satoh, M., Shephard, M.  
832 W., Velázquez-Blázquez, A., Wandinger, U., Wehr, T., and van Zadelhoff, G.-J.: The  
833 Earth CARE Satellite: The Next Step Forward in Global Measurements of Clouds,  
834 Aerosols, Precipitation, and Radiation, *B. Am. Meteorol. Soc.*, 96, 1311–1332,  
835 <https://doi.org/10.1175/BAMS-D-12-00227.1>, 2015.

- 836 Junge, C.E., Chagnon, C.W., and Manson, J.E.: A World-wide Stratospheric Aerosol  
837 Layer, *Science*, 133, 1478-1479, 1961.
- 838 Kablick, G. P., Allen, D. R., Fromm, M. D., and Nedoluha, G. E.: Australian PyroCb Smoke  
839 Generates Synoptic-Scale Stratospheric Anticyclones, *Geophys. Res. Lett.*, 47,  
840 e2020GL08810, <https://doi.org/10.1029/2020GL088101>, 2020.
- 841 Kar, J., Lee, K.-P., Vaughan, M. A., Tackett, J. L., Trepte, C. R., Winker, D. M., Lucker, P. L.,  
842 and Getzewich, B. J.: CALIPSO level 3 stratospheric aerosol profile product:  
843 version 1.00 algorithm description and initial assessment, *Atmos. Meas. Tech.*,  
844 12, 6173–6191, <https://doi.org/10.5194/amt-12-6173-2019>, 2019.
- 845 Kloss, C., Berthet, G., Sellitto, P., Ploeger, F., Taha, G., Tidiga, M., Eremenko, M.,  
846 Bossolasco, A., Jégou, F., Renard, J.-B., and Legras, B.: Stratospheric aerosol  
847 layer perturbation caused by the 2019 Raikoke and Ulawun eruptions and their  
848 radiative forcing, *Atmos. Chem. Phys.*, 21, 535–560, <https://doi.org/10.5194/acp-21-535-2021>, 2021.
- 850 Kovilakam, M., Thomason, L.W., Ernest, N., Rieger, L.A., Bourassa, A.E., and Millán, L.:  
851 The Global Space-based Stratospheric Aerosol Climatology (version 2.0): 1979–  
852 2018, *Earth Syst. Sci. Data*, 12, 2607–2634, <https://doi.org/10.5194/essd-12-2607-2020>, 2020.
- 854 Kovilakam, M., Thomason, L.W., and Knepp, T.: SAGEIII/ISS aerosol/cloud categorization  
855 and its impact on GloSSAC, *Atmos. Meas. Tech.*, 16, 2709–2731,  
856 <https://doi.org/10.5194/amt-16-2709-2023>, 2023.
- 857 Kremser, S., Thomason, L. W., von Hobe, M., Hermann, M., Desher, T., Timmreck, C.,  
858 Toohey, M., Stenke, A., Schwarz, J. P., Weigel, R., Fueglistaler, S., Prata, F. J.,  
859 Vernier, J. P., Schlager, H., Barnes, J. E., Antuña-Marrero, J. C., Fairlie, D., Palm,  
860 M., Mahieu, E., Notholt, J., Rex, M., Bingen, C., Vanhellemont, F., Bourassa, A.,  
861 Plane, J. M. C., Klocke, D., Carn, S. A., Clarisse, L., Trickl, T., Neely, R., James, A.  
862 D., Rieger, L., Wilson, J. C., and Meland, B.: Stratospheric aerosol– Observations,  
863 processes, and impact on climate, *Rev. Geophys.*, 54, 278–335,  
864 <https://doi.org/10.1002/2015RG000511>, 2016.
- 865 Li, C., Krotkov, N.A., Carn, S., Zhang, Y., Spurr, R.D.J., and Joiner, J.: New-generation  
866 NASA Aura Ozone Monitoring Instrument (OMI) volcanic SO<sub>2</sub> dataset: algorithm  
867 description, initial results, and continuation with the Suomi-NPP Ozone Mapping  
868 and Profiler Suite (OMPS), *Atmos. Meas. Tech.*, 10, 445–458, [www.atmos-meas-  
869 tech.net/10/445/2017/](http://www.atmos-meas-tech.net/10/445/2017/), doi:10.5194/amt-10-445-2017, 2017.
- 870 Lin, P., and Fu, Q., Changes in various branches of the Brewer–Dobson circulation from  
871 an ensemble of chemistry climate models, *J. Geophys. Res.*, 118, 73–84,  
872 doi:10.1029/2012JD018813, 2013.
- 873 Malinina, E., Rozanov, A., Niemayer, U., Wallis, S., Arosio, C., Wrana, F., Timmreck, C.,  
874 von Savigny, C., and Burrows, J.P.: Changes in stratospheric aerosol extinction

875 coefficient after the 2018 Ambae eruption as seen by OMPS-LP and MAECHAM5-  
876 HAM, *Atmos. Chem. Phys.*, 21, 14871–14891, [https://doi.org/10.5194/acp-21-](https://doi.org/10.5194/acp-21-14871-2021)  
877 14871-2021, 2021.

878 Martinsson, B. G., Nguyen, H. N., Brenninkmeijer, C. A. M., Zahn, A., Heintzenberg, J.,  
879 Hermann, M., and Velthoven, P. F. J. v.: Characteristics and origin of lowermost  
880 stratospheric aerosol at northern midlatitudes under volcanically quiescent  
881 conditions based on CARIBIC observations, *J. Geophys. Res.*, 110, D12201,  
882 doi:10.1029/2004JD005644, 2005.

883 Martinsson, B. G., Brenninkmeijer, C. A. M., Cam, S. A., Hermann, M., Heue, K.P., van  
884 Velthoven, P. F. J., and Zahn, A.: Influence of the 2008 Kasatochi volcanic  
885 eruption on sulfurous and carbonaceous aerosol constituents in the lower  
886 stratosphere, *Geophys. Res. Lett.*, 36, 1–5,  
887 <https://doi.org/10.1029/2009GL038735>, 2009.

888 Martinsson, B. G., Friberg, J., Sandvik, O. S., Hermann, M., van Velthoven, P. F. J., and  
889 Zahn, A.: Particulate sulfur in the upper troposphere and lowermost  
890 stratosphere– sources and climate forcing, *Atmos. Chem. Phys.*, 17, 10937–  
891 10953, [https://doi.org/10.5194/acp-17-10937-](https://doi.org/10.5194/acp-17-10937-2017)2017, 2017.

892 Martinsson, B. G., Friberg, J., Sandvik, O. S., Hermann, M., van Velthoven, P. F. J., and  
893 Zahn, A.: Formation and composition of the UTLS aerosol, *npj Climate and*  
894 *Atmospheric Science*, 2, 1–6, <https://doi.org/10.1038/s41612-019-0097-1>, 2019.

895 Martinsson, B. G., Friberg, J., Sandvik, O. S., and Sporre, M. K.: Five-satellite-sensor  
896 study of the rapid decline of wildfire smoke in the stratosphere, *Atmos. Chem.*  
897 *Phys.*, 22, 3967–3984, [https://doi.org/10.5194/acp-22-3967-](https://doi.org/10.5194/acp-22-3967-2022)2022, 2022.

898 Martinsson, B. G., Friberg, J., and Sporre, M. K.: Stratospheric aerosol formed by intense  
899 volcanism–sea interaction during the 2022 Hunga Ha’apai eruption, *Atmos.*  
900 *Chem. Phys.*, 25, 10677–10690, [https://doi.org/10.5194/acp-25-10677-](https://doi.org/10.5194/acp-25-10677-2025)2025,  
901 2025.

902 Mastin, L. G., Van Eaton, A. R., and Cronin, S. J.: Did steam boost the height and growth  
903 rate of the giant Hunga eruption plume?, *B. Volcanol.*, 86, 64,  
904 <https://doi.org/10.1007/s00445-024-01749-1>, 2024.

905 McCarthy, G.J., Plucinski, M.P., and Gould, J.S.: Analysis of the resourcing and  
906 containment of multiple remote fires: The Great Divide Complex of fires, Victoria,  
907 December 2006, *Australian Forestry*, 75, 54-63, DOI:  
908 10.1080/00049158.2012.10676385, 2012.

909 Mote, P.W., Dunkerton, T.J., McIntyre, M.E., Ray, E.A., Haynes, P.H., and Russell III, J.M.:  
910 Vertical velocity, vertical diffusion, and dilution by midlatitude air in the tropical  
911 lower stratosphere, *J. Geophys. Res.* 103, 8651-8666, 1998.

912 Murphy, D. M., Cziczo, D. J., Hudson, P. K., and Thomson, D. S.: Carbonaceous material  
 913 in aerosol particles in the lower stratosphere and tropopause region, *J. Geophys.*  
 914 *Res.*, 112, D04203, <https://doi.org/10.1029/2006JD007297>, 2007.

915 NASA/LARC/SD/ASDC: Science CALIPSO Lidar Level 1B profile data, V4-51, NASA  
 916 Langley Atmospheric Data Center DAAC,  
 917 [https://doi.org/10.5067/CALIOP/CALIPSO/CAL\\_LID\\_L1 Standard-V4-51](https://doi.org/10.5067/CALIOP/CALIPSO/CAL_LID_L1 Standard-V4-51), 2024.

918 Nicknish, P.A., Stone, K., Solomon, S., and Carn, S.A.: Quantifying the decay timescale  
 919 of volcanic sulfur dioxide in the stratosphere, *Atmos. Chem. Phys.*, 25, 11535–  
 920 11555, <https://doi.org/10.5194/acp-25-11535-2025>, 2025.

921 Ohneiser, K., Ansmann, A., Baars, H., Seifert, P., Barja, B., Jimenez, C., Radenz, M.,  
 922 Tiesseire, A., Floutsi, A., Haarig, M., Foth, A., Chudnovsky, A., Engelmann, R.,  
 923 Zamorano, F., Bühl, J., and Wandinger, U.: Smoke of extreme Australian bushfires  
 924 observed in the stratosphere over Punta Arenas, Chile, in January 2020: optical  
 925 thickness, lidar ratios, and depolarization ratios at 355 and 532nm, *Atmos.*  
 926 *Chem. Phys.*, 20, 8003–8015, <https://doi.org/10.5194/acp-20-8003-2020>, 2020.

927 Pardini, F., Burton, M., Arzilli, F., La Spina, G., and Polacci, M.: SO<sub>2</sub> emissions, plume  
 928 heights and magmatic processes inferred from satellite data: The 2015 Calbuco  
 929 eruptions, *J. Volcanol. Geotherm. Res.* 361, 12-24, 2018.

930 Peterson, D. A., Fromm, M. D., McRae, R. H. D., Campbell, J. R., Hyer, E. J., Taha, G.,  
 931 Camacho, C. P., Kablick, G. P., Schmidt, C. C., and DeLand, M. T.: Australia's  
 932 Black Summer pyrocumulonimbus super outbreak reveals potential for  
 933 increasingly extreme stratospheric smoke events, *Npj Clim. Atmos. Sci.*, 4, 38  
 934 <https://doi.org/10.1038/s41612-021-00192-9>, 2021.

935 Peterson, D. A., Berman, M. T., Fromm, M. D., Servranckx, R., Julstrom, W. J., Hyer, E. J.,  
 936 Campbell, J. R., McHardy, T. M., and Lambert, A.: Worldwide inventory reveals  
 937 the frequency and variability of pyrocumulonimbus and stratospheric smoke  
 938 plumes during 2013–2023, *Npj Clim. Atmos. Sci.*, 8, 325,  
 939 <https://doi.org/10.1038/s41612-025-01188-5>, 2025.

940 Ploeger, F., Diallo, M., Charlesworth, E., Konopka, P., Legras, B., Laube, J.C., Gross, J.-U.,  
 941 Günther, G., Engel, A., and Riese, M.: The stratospheric Brewer–Dobson  
 942 circulation inferred from age of air in the ERA5 reanalysis, *Atmos. Chem. Phys.*,  
 943 21, 8393–8412, <https://doi.org/10.5194/acp-21-8393-2021>, 2021.

944 Prata, A. T., Young, S. A., Siems, S. T., and Manton, M. J.: Lidar ratios of stratospheric  
 945 volcanic ash and sulfate aerosols retrieved from CALIOP measurements, *Atmos.*  
 946 *Chem. Phys.*, 17, 8599–8618, <https://doi.org/10.5194/acp-17-8599-2017>, 2017.

947 Rieger, L.A., Bourassa, A.E., and Degenstein, D.A.: Merging the OSIRIS and SAGE II  
 948 stratospheric aerosol records, *J. Geophys. Res. Atmos.*, 120, 8890–8904,  
 949 doi:10.1002/2015JD023133, 2015.

- 950 Sandvik, O. S., Friberg, J., Sporre, M. K., and Martinsson, B. G.: Methodology to obtain  
 951 highly resolved SO<sub>2</sub> vertical profiles for representation of volcanic emissions in  
 952 climate models, *At mos. Meas. Tech.*, 14, 7153–7165,  
 953 <https://doi.org/10.5194/amt 14-7153-2021>, 2021.
- 954 Sato, M., Hansen, J.E., McCormick, M.P., and Pollack J.B.: Stratospheric aerosol optical  
 955 depths, 1850-1990, *J. Geophys. Res.* 98, 22987-22994, 1993.
- 956 Schmidt, A., Mills, M. J., Ghan, S., Gregory, J. M., Allan, R. P., Andrews, T., Bardeen, C. G.,  
 957 Conley, A., Forster, P. M., Gettelman, A., Portmann, R. W., Solomon, S., and Toon,  
 958 O. B.: Volcanic radiative forcing from 1979 to 2015, *J. Geophys. Res.-Atmos.*, 123,  
 959 12491–12508, <https://doi.org/10.1029/2018JD028776>, 2018.
- 960 Seabrook, S., Mackay, K., Watson, S. J., Clare, M. A., Hunt, J. E., Yeo, I. A., Lane, E. M.,  
 961 Clark, M. R., Wysoczanski, R., Rowden, A.A., Kula, T., Hoffmann, L.J., Armstrong,  
 962 E., and Williams, M. J. M.: Volcaniclastic density currents explain widespread  
 963 and diverse seafloor impacts of the 2022 Hunga Volcano eruption, *Nat.*  
 964 *Commun.*, 14, 7881, <https://doi.org/10.1038/s41467-023-43607 2>, 2023.
- 965 Sheng, J.-X., Weisenstein, D.K., Luo, B.-P., Rozanov, E., Stenke, A., Anet, J., Bingemer, H.,  
 966 and Peter, T.: Global atmospheric sulfur budget under volcanically quiescent  
 967 conditions: Aerosol-chemistry-climate model predictions and validation, *J.*  
 968 *Geophys. Res. Atmos.*, 120, 256–276, doi:10.1002/2014JD021985, 2015.
- 969 Solomon, S., Daniel, J. S., Neely, R. R., Vernier, J.-P., Dutton, E. G., and Thomason, L. W.:  
 970 The persistently variable “background” stratospheric aerosol layer and global  
 971 climate change, *Science*, 333, 866–870, 2011.
- 972 Solomon S., Dube K., Stone K., Yu P., Kinnison D., Toon O.B., Strahan S.E., Rosenlov  
 973 K.H., Portmann R., Davis S., Randel W., Bernath P., Boone C., Bardeen C.G.,  
 974 Bourassa A., Zawada D., and Degenstein D.: On the stratospheric chemistry of  
 975 midlatitude wildfire smoke, *Proc. Natl. Acad. Sci. U.S.A.* 119, E2117325119,  
 976 <https://doi.org/10.1073/pnas.2117325119>, (2022).
- 977 Surano, Jousset, P., Pallister, J., Boichu, M., Bongiorno, M.F., Budisantoso, A., Costa, F.,  
 978 Andreastuti, S., Prata, F., Schneider, D., Clarisse, L., Humaida, H., Sumarti, S.,  
 979 Bignami, C., Griswold, J., Carn, S., Oppenheimer C., and Lavigne F.: The 2010  
 980 explosive eruption of Java's Merapi volcano—A ‘100-year’ event, *J. Volcanol.*  
 981 *Geotherm. Res.* 241-242, 121-135, 2012.
- 982 Taylor, I. A., Grainger, R. G., Prata, A. T., Proud, S. R., Mather, T. A., and Pyle, D. M.: A  
 983 satellite chronology of plumes from the April 2021 eruption of La Soufrière, St  
 984 Vincent, *Atmos. Chem. Phys.*, 23, 15209–15234, <https://doi.org/10.5194/acp-23-15209 2023>, 2023.
- 986 Thomas, H.E., Watson, I.M., Carn, S.A., Prata, A.J., and Realmuta, V.J.: A comparison of  
 987 AIRS, MODIS and OMI sulphur dioxide retrievals in volcanic clouds, *Geomatics,*  
 988 *Natural Hazards and Risk*, 2, 217-232, 2011.

989 Thomason, L.W., Ernest, N., Millán, L., Rieger, L., Bourassa, A., Vernier, J.-P., Manney, G.,  
990 Luo, B., Arfeuille, F., and Peter, T.: A global space-based stratospheric aerosol  
991 climatology: 1979-2016, *Earth Syst. Sci. Data*, 10, 469–492,  
992 <https://doi.org/10.5194/essd-10-469-2018>, 2018.

993 Vernier, J.-P., Pommereau, J.P., Garnier, A., Pelon, J., Larsen, N., Nielsen, J.,  
994 Christiansen, T., Cairo, F., Thomason, L.W., Leblanc, T., and McDermid, I.S.:  
995 Tropical stratospheric aerosol layer from CALIPSO lidar observations, *J.*  
996 *Geophys. Res.*, 114, D00H10, doi:10.1029/2009JD011946, 2009.

997 Vernier, J.-P., Farlie, T.D., Murray, J.J., Tupper, A., Trepte, C., Winker, D., Pelon, J., Garnier,  
998 A., Jumelet, J., Pavolonis, M., Omar, A.H., and Powell, K.A.: An Advanced System  
999 to Monitor the 3D Structure of Diffuse Volcanic Ash Clouds *J. Appl. Meteorol.*  
1000 *Clim.* 10, 2125-2138, 2013.

1001 Vernier, J.-P., Farlie, T.D., Natarajan, M., Wiengold, F.G., Bian, J., Martinsson, B.G.,  
1002 Crumeyrolle, S., Thomason, L.W., and Bedka, K.M.: Increase in upper  
1003 tropospheric and lower stratospheric aerosol levels and its potential connection  
1004 with Asian pollution, *J. Geophys. Res.*, 120, doi:10.1002/2014JD022372, 2015.

1005 Weisenstein, D.K., Yue, G.K., Ko, M.K.W., Sze, N.-D., Rodriguez, J.M., and Scott, C.J.: A  
1006 two-dimensional model of sulfur species and aerosol, *J. Geophys. Res.* 102,  
1007 13019-13035, 1997.

1008 Winker, D. M., Hunt, W. H., and McGill, M. J.: Initial performance assessment of CALIOP,  
1009 *Geophys. Res. Lett.*, 34, 1–5, <https://doi.org/10.1029/2007GL030135>, 2007.

1010 Winker, D. M., Pelon, J., Coakley, J. A., Ackerman, S. A., Charlson, R. J., Colarco, P. R.,  
1011 Flamant, P., Fu, Q., Hoff, R. M., Kittaka, C., Kubar, T. L., Le Treut, H., McCormick,  
1012 M. P., Mégie, G., Poole, L., Powell, K., Trepte, K., Vaughan, M. A., and Wielicki, B.  
1013 A.: The CALIPSO mission—A global 3D view of aerosols and clouds, *B. Am.*  
1014 *Meteorol. Soc.*, 91, 1211–1229, <https://doi.org/10.1175/2010BAMS3009.1>, 2010.

1015 *Data availability.* The data used are publicly available: CALIOP V4.51 lidar data  
1016 (<https://search.earthdata.nasa.gov/search?fp=CALIPSO>).

1017 *Author contributions.* BGM planned the study, undertook most of the data analysis and  
1018 wrote the paper. JF participated in the planning of the study, undertook part of the data  
1019 analysis and MKS contributed. JF and MKS undertook data extraction and handling for  
1020 the data analysis. All authors participated in discussions and commented on the  
1021 manuscript.

1022 *Disclaimer.* The contact author and the co-authors declare that they have no competing  
1023 interests.

1024 *Acknowledgements.* Aerosol products from the CALIOP sensor were produced by NASA  
1025 Langley Research Center.

1026 *Financial support.* The Swedish National Space Agency, contracts 2025-00200 and  
1027 2022-00157, Johan Friberg. The Crafoord Foundation, contract 20240901, Johan Friberg.  
1028 Formas, contract 2025-01869, Johan Friberg. Formas, contract 2020-00997, Moa  
1029 Sporre. The Swedish Research Council 2022-02836, Moa Sporre.